AFRL-AFOSR-JP-TR-2024-0020

Single Quantum Emitters based on Strained Quantum Dots in Two-dimensional Semiconductors

Nam, SungWoo
UNIVERSITY OF ILLINOIS
506 S WRIGHT ST
URBANA, IL, 61801
USA

12/12/2023
Final Technical Report

Air Force Research Laboratory
Air Force Office of Scientific Research
Asian Office of Aerospace Research and Development
Unit 45002, APO AP 96338-5002

REPORT DOCUMENTATION PAGE

PLEASE DO NOT RETURN YOUR FORM TO THE ABOVE ORGANIZATION.

1. REPORT DATE	2. REPORT TYPE	3. DATES COVERED	
20231212	Final	START DATE 20170802	END DATE 20210801

4. TITLE AND SUBTITLE
Single Quantum Emitters based on Strained Quantum Dots in Two-dimensional Semiconductors

5a. CONTRACT NUMBER	5b. GRANT NUMBER	5c. PROGRAM ELEMENT NUMBER
	FA2386-17-1-4071	61102F
5d. PROJECT NUMBER	**5e. TASK NUMBER**	**5f. WORK UNIT NUMBER**

6. AUTHOR(S)
SungWoo Nam

7. PERFORMING ORGANIZATION NAME(S) AND ADDRESS(ES)
UNIVERSITY OF ILLINOIS
506 S WRIGHT ST
URBANA, IL 61801
USA

8. PERFORMING ORGANIZATION REPORT NUMBER

9. SPONSORING/MONITORING AGENCY NAME(S) AND ADDRESS(ES)	10. SPONSOR/MONITOR'S ACRONYM(S)	11. SPONSOR/MONITOR'S REPORT NUMBER(S)
AOARD UNIT 45002 APO AP 96338-5002	AFRL/AFOSR IOA	AFRL-AFOSR-JP-TR-2024-0020

12. DISTRIBUTION/AVAILABILITY STATEMENT
A Distribution Unlimited: PB Public Release

13. SUPPLEMENTARY NOTES

14. ABSTRACT
Quantum confinement in atomically-thin transition-metal dichalcogenides (TMDs) has been explored recently for single quantum emitters based on naturally occurring or artificially created defects. In this project, PIs Nam and Park aim to advance our understanding of artificial quantum emitters of atomically-thin TMDs on their emission properties by investigating the effect of deterministic straining and confinement, as opposed to unintentional defects. We propose that mechanical straining and confinement in monolayer TMDs are viable solutions to produce precisely controlled single quantum emitters. In our system, localized (or confined) excitons arise from a confinement potential caused by a local strain gradient. In addition, the two-dimensional (2D) nature of a single quantum emitter confined to an atomically-thin material can greatly enhance the photon-extraction efficiency. Our collaborative team has demonstrated that heterogeneous straining of 2D TMDs (with a localized strain level of 0-4%) can induce efficient exciton funneling across microns at room temperature. Moreover, we showed that localized deformation of 2D TMDs on nanogap can lead to single photon emission with deterministic position and polarization. With the support of AOARD and IITP, PIs Nam and Park published a total of 20 papers in high impact journals, including Nature Electronics, Advanced Materials, Materials Today, etc. We also published two collaborative papers ? (1) polarization-controlled single photon emission of strained WSe2 in Nano Letters and (2) crumpled graphene induced plasmon resonance in Light: Science & Applications. We predict that as the scale of deformation approaches that of exciton Bohr radius, the strained and confined 2D excitons will result in an efficient, single-photon source based on strained 2D semiconductors for next generation, scalable quantum cryptography.

15. SUBJECT TERMS

16. SECURITY CLASSIFICATION OF:			17. LIMITATION OF ABSTRACT	18. NUMBER OF PAGES
a. REPORT U	b. ABSTRACT U	c. THIS PAGE U	SAR	29

19a. NAME OF RESPONSIBLE PERSON	19b. PHONE NUMBER *(Include area code)*
CHRISTOPHER VERGIEN	315-227-7002

Standard Form 298 (Rev.5/2020)
Prescribed by ANSI Std. Z39.18

Final Report for AOARD FA2386-17-1-4071 & IITP 2017-0-00575

Single Quantum Emitters based on Strained Quantum Dots in Two-dimensional Semiconductors

6/30/2021

Name of Principal Investigators (PIs):

Dr. SungWoo Nam (USPI)
- e-mail address: swnam@illinois.edu
- Institution: University of Illinois at Urbana-Champaign (UIUC)
- Mailing Address: 1206 W. Green St., MC-244, Urbana, IL 61801
- Phone: 1-217-300-0267
- Fax: 1-217-244-6534

Dr. Hong-Gyu Park (KPI)
- e-mail address: hgpark@korea.ac.kr
- Institution: Korea University (KU)
- Mailing Address: 145 Anam-ro, Seongbuk-gu, Seoul, South Korea
- Phone: 82-2-3290-3524
- Fax: 82-2-3290-3589

Period of Performance: 8/2/2017 – 6/30/2021

Abstract: Quantum confinement in atomically-thin transition-metal dichalcogenides (TMDs) has been explored recently for single quantum emitters based on naturally occurring or artificially created defects. In this project, PIs Nam and Park aim to advance our understanding of artificial quantum emitters of atomically-thin TMDs on their emission properties by investigating the effect of deterministic straining and confinement, as opposed to unintentional defects. We propose that mechanical straining and confinement in monolayer TMDs are viable solutions to produce precisely controlled single quantum emitters. In our system, localized (or confined) excitons arise from a confinement potential caused by a local strain gradient. In addition, the two-dimensional (2D) nature of a single quantum emitter confined to an atomically-thin material can greatly enhance the photon-extraction efficiency. Our collaborative team has demonstrated that heterogeneous straining of 2D TMDs (with a localized strain level of 0-4%) can induce efficient exciton funneling across microns at room temperature. Moreover, we showed that localized deformation of 2D TMDs on nanogap can lead to single photon emission with deterministic position and polarization. With the support of AOARD and IITP, PIs Nam and Park published a total of 20 papers in high impact journals, including *Nature Electronics*, *Advanced Materials*, *Materials Today*, etc. We also published two collaborative papers − (1) polarization-controlled single photon emission of strained WSe_2 in *Nano Letters* and (2) crumpled graphene induced plasmon resonance in *Light: Science & Applications*. We predict that as the scale of deformation approaches that of exciton Bohr radius, the strained and confined 2D excitons will result in an efficient, single-photon source based on strained 2D semiconductors for next generation, scalable quantum cryptography.

Introduction: The single photon source is one of the most important building blocks in quantum information and quantum cryptography for preventing information leakage[1]. Solid-state single-photon emitters, such as semiconductor quantum dots[2,3] and atomic defects in wide-bandgap materials[4–9], have attracted considerable attention because of the possibility of scaling quantum systems through wafer-scale growth and fabrication[10,11]. The performance of single photon emitters can be improved by integrating them with well-designed optical cavities and increasing the Purcell factor[12]. A high Purcell factor requires not only spatial and spectral matching but also polarization matching between the emitters and cavities. For example, to realize spatial and/or polarization matching of single photon emitters with optical cavities, site-controlled growth[13], high-energy ion implantation[14,15], and high-power laser pulses[16] have been employed, but these techniques still exhibited low yields.

More recently, quantum confinement in atomically thin transition metal dichalcogenides

(TMDCs) has been investigated for single photon emission based on naturally or artificially occurring defects[17–19]. In particular, the precise control of the position of a single photon emitter by applying mechanical strains to the TMDC monolayer is feasible[20–23]. Strains have been induced in TMDCs using various nanostructures including dielectric pillars[20], nanobubbles[21], optical waveguide[22], and metal nanogaps[23]. However, even in such TMDC-based single photon sources, polarization control and integration with a high-quality (Q) cavity to increase the Purcell factor remain as significant challenges. In addition, experimental demonstration of 2D exciton funneling has been limited to indirect evidence such as photoluminescence (PL) enhancement[24–27], comparison of spectral shifts[28] or spatial profiles[29], and PL emission center shift in spatiotemporally resolved PL[30]. Furthermore, it is unclear if limited observations of strain-induced 2D exciton funneling is a result of the inherently short ambient lifetime of 2D intralayer excitons or extrinsic factors such as insufficient strain and sub-diffraction strain gradient. Accordingly, quantitative elucidation of how efficiently strain can induce exciton funneling and what physical parameters should be considered for practical design of strain-induced optoelectronic devices remain elusive thus far.

In this project, the PIs collaboratively investigated (1) strain-engineered exciton funneling in monolayer tungsten diselenide (WSe_2) using pump-probe measurements at ambient temperature, and (2) precise and deterministic control of both the position and polarization of single photon sources formed in monolayer WSe_2 at low temperature. First, we employed three-dimensional soft wrinkle architecture to create optically-resolvable lateral strain gradient from the apex (tensile) to the valley (compressive) of WSe_2 wrinkles. We observed strong influence of strain gradient on exciton decay dynamics as a result of funneling of bright excitons and conversion from dark to bright excitons under varying local strain. Furthermore, strain-induced exciton funneling over micrometer scale distances with high transport efficiency was demonstrated via pump-probe characterization, corroborated with the theoretical strain-exciton coupling model. Second, we achieved band engineering and single photon generation at a desired position by applying a strain to monolayer WSe_2 using a Si_3N_4 rod structure with a nanogap. The polarization of single photons was successfully controlled by changing the nanogap size. Furthermore, we combined emitters with a high-Q photonic crystal cavity to demonstrate a practical single photon source for quantum communication. Our work presents new opportunities for a deterministic and scalable single photon source as well as quantum straintronic devices[31] and quantum excitonic phase transitions[32–36].

Experiment:
(1) Preparation, characterization and theory of strained two-dimensional semiconductors

Sample preparation
Monolayer tungsten diselenide (WSe_2) was mechanically exfoliated from single crystalline bulk WSe_2 (HQ Graphene, Netherlands). We first prepared a polydimethylsiloxane (PDMS) substrate by mixing base elastomer and curing agent (Sylgard 184, Dow Corning Incorporation) and curing at 70 °C for 60 min. Then, we prestretched a PDMS substrate with 20% of prestrain, followed by oxidizing PDMS surface with oxygen plasma treatment to form stiff silica skin layer on top of PDMS. We then prepared exfoliated 1L-WSe_2 and transferred it to silica/PDMS substrate with polymethyl methacrylate (PMMA) as supporting film on WSe_2. Afterward we slowly removed prestrain of PDMS. For two-point bending measurement, we transferred PMMA/WSe_2 on 500 μm-thick polycarbonate (PC) substrate.

Structural and optical characterization
Geometry of wrinkle structure was characterized by atomic force microscope (AFM) (Cypher, Asylum Research, CA, USA) and 3D laser scanning confocal microscope (VK-ZX1000, Keyence, Japan). The thickness of oxidized silica layer on PDMS was measured by X-ray reflectivity (XRR) (PANalytical Philips X'pert MRD diffractometer, USA) using Cu K α radiation (λ = 0.154056 nm). Photoluminescence (PL)/Raman point spectra and line profiles were obtained by Raman confocal imaging microscope (LabRAM HR, Horiba, Japan) and PL area map was measured by confocal Raman microscope (Nanophoton Raman 11, Nanophoton Corporation, Japan) equipped with line illumination. All the PL/Raman measurements were performed with 532 nm excitation laser.

Time-resolved PL (TRPL) and pump-probe measurements were carried out using a home-built fiber-coupled confocal microscope (Fig. 1). The setup was composed of two sets of two-dimensional galvo mirror scanning systems in order to control the pump and the probe positions respectively. A pulsed red laser (632 nm) was used for excitation in TRPL measurement and a continuous green laser

(532 nm) was used for excitation in pump-probe measurement. The beam was focused through a 100x objective with a numerical aperture (NA) of 0.9. The detection signal was focused into a single mode fiber. A fiber splitter then led the coupled signal either to a spectrometer (Acton SpectraPro™, Princeton Instrument Inc.) for spectral measurements or to an avalanche photodiode (APD; Excelitas SPCM AQRH 13). The time-correlated-single-photon-counting (TCSPC, PicoHarp300) was used to obtain the time resolved PL. For low temperature PL measurement, the sample was mounted in a vibration-isolated cryostat cooled by compressed helium and a 50x microscope objective lens (NA 0.42) was used for confocal PL setup similar to the room temperature measurement.

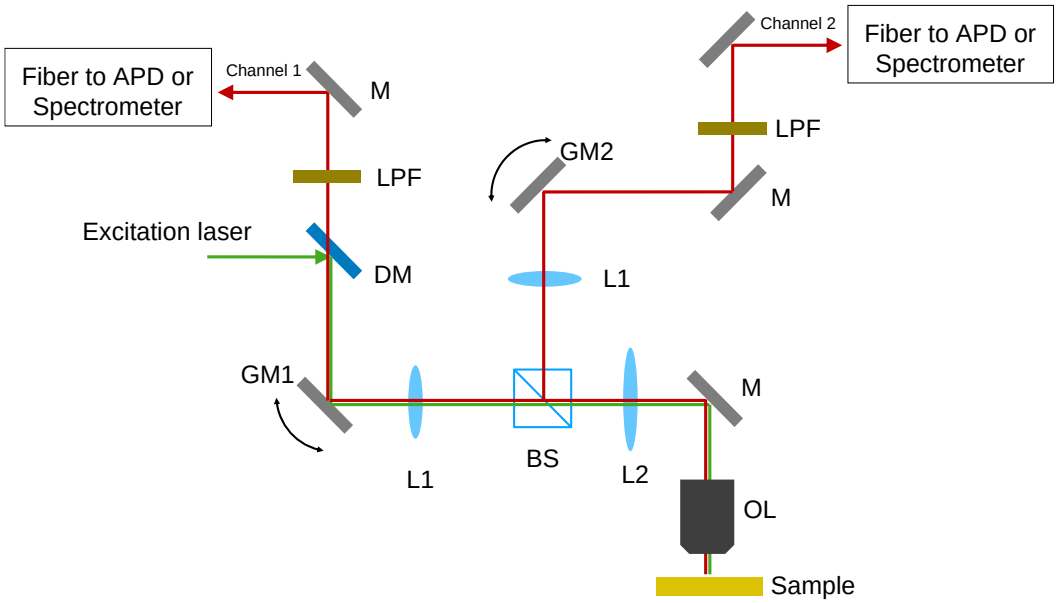

Fig. 1. Confocal pump-probe measurement setup. M: Mirror, GM1 and GM2: Galvo mirrors, L1 and L2: Lens, BS: Beam splitter, DM: Dichroic mirror, OL: Objective lens, LPF: Long pass filter.

Exciton decay simulation

To explain the trend of PL decay under heterogeneous local strain, we employed a spatiotemporal exciton continuity equation as described below:

$$\frac{\partial n_b}{\partial t} = -\frac{n_b}{\tau_b} - \eta n_b^2 + D\nabla^2 n_b + \mu_b \gamma_b \nabla\left(n_b\left(\nabla\varepsilon\right)\right) - C_{bd}\left(n_b - n_d \exp\left(\frac{\Delta E_{bd}}{k_B T}\right)\right) \quad (1)$$

$$\frac{\partial n_d}{\partial t} = -\frac{n_d}{\tau_d} - \eta n_d^2 + D\nabla^2 n_d + \mu_d \gamma_d \nabla\left(n_d\left(\nabla\varepsilon\right)\right) + C_{bd}\left(n_b - n_d \exp\left(\frac{\Delta E_{bd}}{k_B T}\right)\right) \quad (2)$$

where subscripts b and d refer to bright and dark excitons respectively, n is the exciton density, t is time, τ is exciton lifetime, η is the exciton-exciton annihilation constant, D is diffusivity, μ is mobility, γ is the strain sensitivity of exciton energy, ε is applied strain, C_{bd} is the dark-to-bright exciton conversion coefficient, ΔE_{bd} is the energy difference between bright and dark excitons, k_B is the Boltzmann constant, and T is temperature. ε was estimated from the PL shift allowing us to set local strain at the apex and valley of wrinkles. For calculation of the strain gradient, $\nabla\varepsilon$, the strain profile across wrinkle structure was approximated as having an ~$\sin^4(\pi x/\lambda)$ form, where λ is wrinkle wavelength, based on the steep strain gradient near apex than valley in PL/Raman profile. In the case of flat structures strain is assumed to be uniformly 0%. Excitation at t = 0 is assumed to follow 2D Gaussian distribution (σ^2 = 0.2 μm^2) and generated excitons. For both bright and dark excitons, the exciton-exciton annihilation constant, η (0.36 cm^2 s^{-1})[37], and exciton diffusivity, D (2 cm^2 s^{-1})[38], are assumed to be identical. Concerning parameters which diverge between bright and dark excitons, bright exciton behavior is well reported allowing us to extract bright exciton mobility, μ_b (300 cm^2 V^{-1} s^{-1})[30], and strain sensitivity of energy, γ_b (49 meV/%strain)[39], from the literature. In contrast, dark exciton mobility, μ_d, and strain sensitivity of energy, γ_d, have not been explicitly reported, requiring estimation from the values for bright excitons. The mobility of Q-valley charge transport is less than

1/20 of K-valley mobility due to strong phonon scattering at Q-valley, resulting in negligible contribution of dark exciton drift[40]. Similarly, the strain sensitivity of dark excitons, $\gamma_{d,}$ in monolayer WSe_2 is approximately one fifth of that of bright excitons, γ_b, with opposite sign, allowing estimation of γ_d (e.g., γ_d / γ_b = -0.22 (uniaxial strain)[39] or -0.25 (biaxial strain)[41]).

In addition to inherent exciton behavior, we need to account for exciton lifetime, τ. Focusing on bright excitons, the delay in radiative recombination of bright excitons due to drift momentum is given by (3)[42].

$$\tau_b(Q) = \frac{\tau_b(0)}{1-\left(\frac{cQ}{E(Q)}\right)^2} \qquad (3)$$

where Q is exciton momentum, $\tau_b(Q)$ is radiative lifetime of bright exciton with momentum Q, and c is speed of light. For exciton decay time with zero drift-momentum (i.e., flat WSe_2), we obtained three exponential components from the TRPL curves. Drift momentum was derived from drift velocity according to the Drude model. For the non-radiative decay of dark excitons (τ_d), there are no reported experimental or theoretical estimations, but the ratio of non-radiative decay of spin-forbidden dark excitons to radiative decay is reported to be more than 50[43], implying much slower decay of optically-forbidden transition state compared to radiative direct transition. In our calculation, we assumed ten times longer decay time of non-radiative, momentum-forbidden dark exciton vs. radiative decay time.

Finally, it is possible for dark excitons to convert to bright excitons requiring us to determine the dark-to-bright exciton energy difference, ΔE_{bd}, and the dark-to-bright exciton conversion coefficient, $C_{bd.}$ We chose $\Delta E_{bd}(\varepsilon=0)$ = -60 meV based on recent first principles calculations[44]. Energy difference at nonzero strain, $\Delta E_{bd}(\varepsilon)$, was determined from $\Delta E_{bd}(\varepsilon=0)$ by correcting for local strain using the strain sensitivity of bright/dark excitons (γ_b/γ_d). The phonon scattering rate for dark-to-bright conversion (C_{bd}) has not been reported yet, so was used as a fitting parameter for recreation of the TRPL curves. Using the above parameters, we solved (1) and (2) numerically using Mathematica software.

(2) Preparation, characterization and theory of position and polarization controlled WSe_2 single photon emitters

Sample preparation

To experimentally demonstrate the array of single photon emitters, we first fabricated Si_3N_4 rod structures with different gaps (d) and widths (w). Rod structures were fabricated on a 150-nm-thick Si_3N_4/1-μm-thick SiO_2/Si substrate wafer. A 20-nm-thick Cr mask was defined on the wafer via electron-beam lithography, electron-beam evaporation, and lift-off processes. Reactive ion etching was performed to etch the Si_3N_4 layer, and subsequently the Cr mask was removed using a Cr etchant (Sigma Aldrich). Then, mechanically exfoliated WSe_2 monolayer flakes were transferred onto the fabricated Si_3N_4 rod structure using a PDMS (GelPak) stamping method.

To integrate a single photon emitter with a cavity, we first fabricated photonic crystal structures on a 200-nm-thick Si_3N_4/1-μm-thick SiO_2/Si substrate wafer using electron-beam lithography and reactive ion etching. Three-cell photonic crystal nanobeam cavities were defined with a lattice constant of 280 nm, a regular hole diameter of 195 nm, and a reduced hole diameter of 95 nm. The slab thickness and width of the nanobeam structure were 200 and 420 nm, respectively. The sacrificial SiO_2 layer underneath the Si_3N_4 layer was selectively wet etched using a buffered oxide etchant solution. Then, the free-standing Si_3N_4 photonic crystal slab was transferred to the strained monolayer WSe_2 by transfer printing method using a PDMS tip.

Optical measurement

A 532-nm continuous-wave solid-state laser (Coherent OBIS) was used to optically pump the sample in a He-flow cryostat (Montana Instruments s50) with the temperature varying from 4 K to room temperature. For high-resolution fast raster scans, two scanning galvo mirrors were used with a 4-f confocal alignment system. The PL emission from the sample was collected by a 100× objective lens with a numerical aperture of 0.85 and sent to either a monochromator/CCD (Princeton Instruments PIXIS 400 BRX) or avalanche photodiodes (Excelitas SPCM AQRH 13).

For photon statistics measurements, we constructed an HBT setup (Fig. 2). After spectral filtering using band-pass filters with various bandwidths, the light emitted from a single photon source was

coupled to an optical fiber and split into two paths using a non-polarizing 50:50 fiber beam splitter. The photons were detected by two identical avalanche photodiodes and time tagging electronics (PicoQuant Picoharp 300). To perform polarization-resolved measurements, a linear polarizer was placed in front of the fiber coupler.

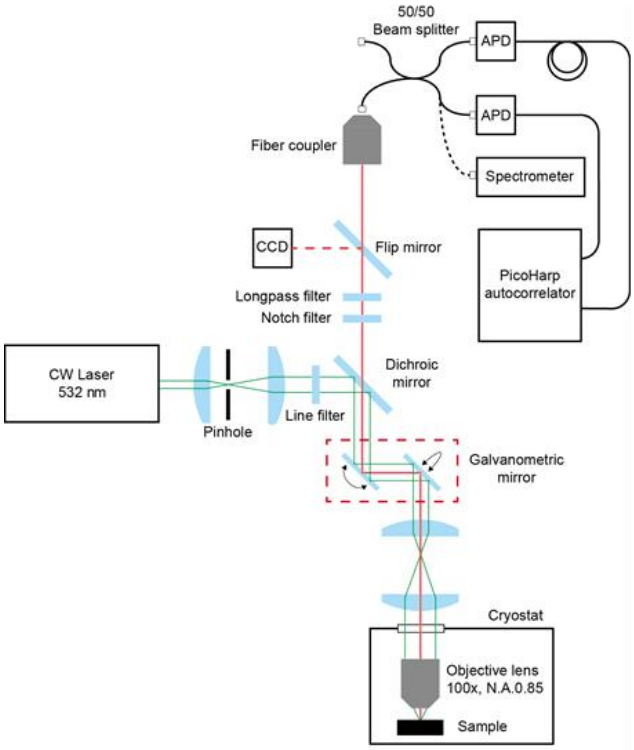

Fig 2. Optical measurement setup. The pump beam (green line) of a 532-nm continuous-wave laser was focused on the sample using a 100× objective lens with a numerical aperture of 0.85, and the sample was scanned using a two-axis galvanometric mirror assembly. The sample, which was mounted on a piezoelectric motorized stage, and the objective lens were inside a cryostat with varying temperatures. The light emission from the sample (red line) was collected by the same objective lens and fed into either a visible CCD for imaging or a fiber coupler for measurements of the photon counts, spectrum, and photon correlation function. Long-pass and notch filters were placed in front of the CCD and fiber coupler, to cut off the pump beam reflected from the sample.

Numerical simulation

Mechanical contact simulations were performed using the FEM (COMSOL Multiphysics, structural mechanics module) to calculate the deformation of the PDMS (Fig. 3). The material properties of the PDMS were described using the Neo-Hookean hyperelastic material model: the density was 970 kg/m^3, the Lamé parameter λ was 6.93 GPa, and the Lamé parameter μ was 0.77 GPa. The Si_3N_4 rod was assumed to be incompressible. The structural parameters of the rod structure were determined according to the fabricated sample: the height and width were 150 and 100 nm, respectively, and the radius of curvature of the top and side edges near the nanogap were 10 and 30 nm, respectively. Two nanogap sizes of 60 to 140 nm were examined. To calculate the deformation of the PDMS, the PDMS was pressed to the rod from $z = 0$ to -150 nm with $\Delta z = 1.5$ nm, where z represents the height of the PDMS and $z = 0$ when the PDMS starts to contact the rod. Then, we traced the morphology of the PDMS and obtained the results of Fig. 3. at $z = -37.5$ nm.

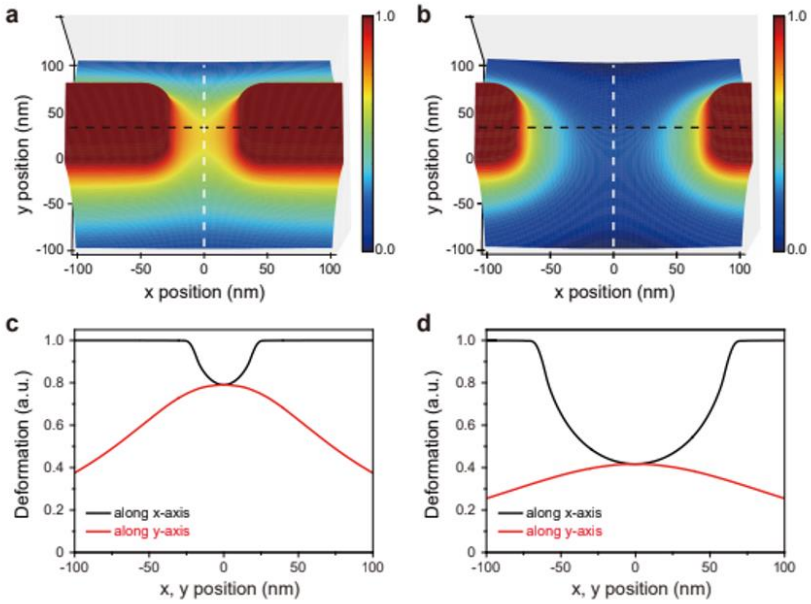

Fig. 3. Simulation of morphology of pressed PDMS. a-b, Three-dimensional simulated morphology of the PDMS pressed onto the narrow (a) and wide (b) nanogaps. The values of *d* and *w* were 60 and 100 nm, respectively (a) and 140 and 100 nm, respectively (b). **c-d,** Deformation taken from **a** (c) and **b** (d) along the x-axis (black dashed lines in a and b) and y-axis (white dashed lines in a and b). The deformation was normalized by the maximum height at x = ±100 nm and y = 0 nm.

Results and Discussion:

(1) Controlled exciton transport in strained two-dimensional semiconductors

Heterogeneous straining of wrinkled 2D semiconductors

Our wrinkle architecture consists of an elastomeric substrate with multiple functional hetero-layers (Fig. 4a). Exfoliated monolayer WSe_2 was transferred to a prestretched silica/polydimethylsiloxane (PDMS) substrate with polymethyl methacrylate (PMMA) encapsulation, and the PDMS was slowly released to form wrinkles in WSe_2. We used stiff silica skin layers to guide conformal deformation of the WSe_2 during substrate contraction while exhibiting stronger van der Waals interaction with WSe_2 than clean elastomeric substrates[45,46]. We further utilized encapsulating PMMA top layer to prevent slippage or delamination of the WSe_2 layer which can reduce local strain.

We first investigated the geometry-dependent local strain modulation of our wrinkled WSe_2 structure. As shown in the optical microscope image (Fig. 4b) and height profile of wrinkled WSe_2, a periodic wrinkle geometry was formed with an average height of 1.25 ± 0.08 μm and an average wrinkle wavelength of 4.84 ± 0.64 μm. In addition, we measured PL emission and plotted the PL peak wavelength map (Fig. 4c). This map clearly shows that the PL emission of wrinkled WSe_2 is periodically modulated in correlation with the fabricated wrinkles. More specifically, the PL spectrum measured at the apex and valley of the wrinkles (Fig. 4d) indicates PL red-shift at apex (ΔE = -88 meV) and blue-shift at valley (ΔE = 20 meV) relative to the exciton energy of flat WSe_2 (E = 1.671 eV) due to tensile and compressive strains respectively. This PL shift was consistently observed across in 147 apexes and 140 valleys from 15 different samples. The histogram of exciton energy distribution shows an average energy at apex and valley of 1.574 ± 0.014 eV and 1.693 ± 0.012 eV, respectively (Fig. 4e). The average strain difference between apex (tensile) and valley (compressive) was calculated to be 2.4 ± 0.3%, on the basis of uniaxial strain sensitivity of monolayer WSe_2 A exciton[39]. Furthermore, Fig. 4f displays the Raman and PL spectra sequentially obtained along the line in Fig. 4c. The spatial coincidence between Raman and PL shift indicates that the observed PL shift originates from the lattice strain. The strong PL enhancement at the wrinkle apex gives indirect evidences of exciton funneling[24,25], after correcting for confounding factors affecting PL/Raman intensities including different focal plane and local curvature. Additionally, the local strain value here exceeds those previously achieved by strain engineering of monolayer TMDCs[25,30,39,47]. We attribute such a high strain to conformal deformation of 2D layers with stiff silica layer and restriction of interfacial

slip by encapsulation with PMMA. Consequently, the well-defined and consistent micrometer-scale strain offers optically-resolvable strain gradient for more accurate optical characterization of exciton funneling behavior.

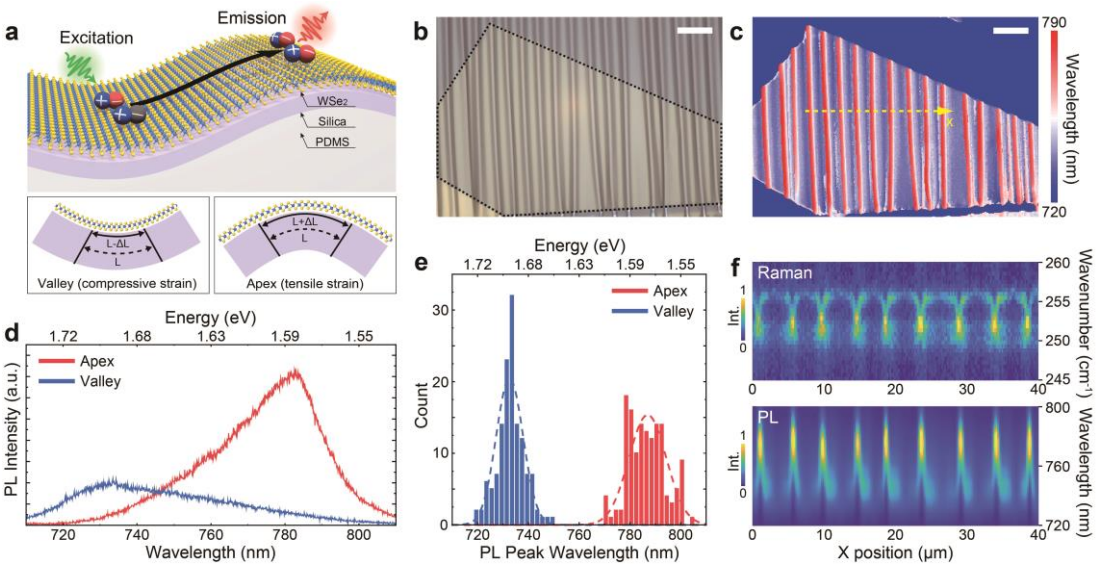

Fig. 4. Heterogeneous exciton engineering of monolayer WSe_2 via soft wrinkle architecture. a, Schematic diagram of mechanically reconfigurable wrinkle architecture made of multiple thin films on PDMS including silica skin layer, WSe_2, and encapsulating PMMA layer (not shown in the schematic). Tensile and compressive strain are applied to WSe_2 at apex and valley of the wrinkle architecture, respectively. **b,** Optical microscope image of wrinkled monolayer WSe_2 (dotted outline). **c,** PL peak wavelength mapping. The scale bars in (b) and (c) are 10 μm. **d,** PL emission spectra measured from WSe_2 at apex (red) and valley (blue). **e,** Statistical analysis on PL shift of wrinkled WSe_2 in 15 different samples with 147 apexes and 140 valleys. Dashed lines are Gaussian fitting of histogram data. **f,** (Top) Raman line mapping along the yellow line in (c). (Bottom) PL line mapping along the same line.

Next, we examined the tunability of local strain by tailoring wrinkle architecture both statically and dynamically. For static control, prestrain, modulus, and thickness of the skin and encapsulating layer can be tuned. For instance, a different degree of PL energy shift was measured with varying skin layer thickness (Fig. 5). In addition, mechanical reconfiguration of local strain was demonstrated by (re)stretching and releasing the PDMS substrate to vary wrinkle height and wavelength (Fig. 6). Initial release of prestrain (ε_{PDMS} = 20%) caused formation of wrinkle structure and strain-induced PL shift, while restretching the PDMS (ε_{PDMS} = 18%) induced significant drop of PL shift (approximately 27% of initial PL shift) and delocalized PL emission. Releasing stretched PDMS led to a recovery of PL shift and localized PL emission at apex. A cyclic stretching test up to 1,000 cycles showed that strain difference at the apex and valley returned to 92% of initial strain after 1,000 cycles (Fig. 7). These results indicate that our soft wrinkle architecture enables structural tunability and mechanical reconfigurability for control of local strain.

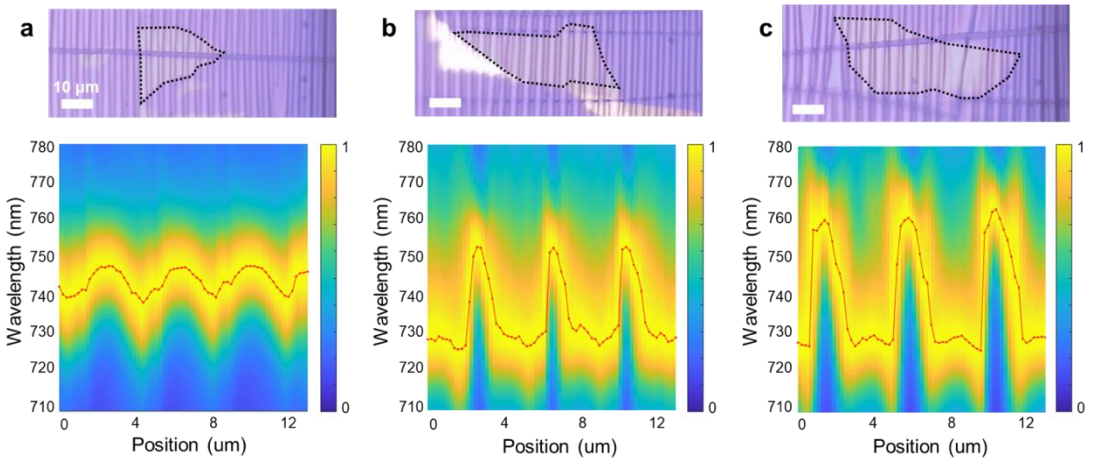

Fig. 5. Tunable wrinkle architecture by changing thickness of silica skin layer. Different oxygen plasma treatments for 1 min (a), 2 min (b), and 3 min (c) induce silica layer on PDMS to be 11.1 nm, 12.1 nm, and 14.7 nm estimated by X-ray reflectivity analysis.

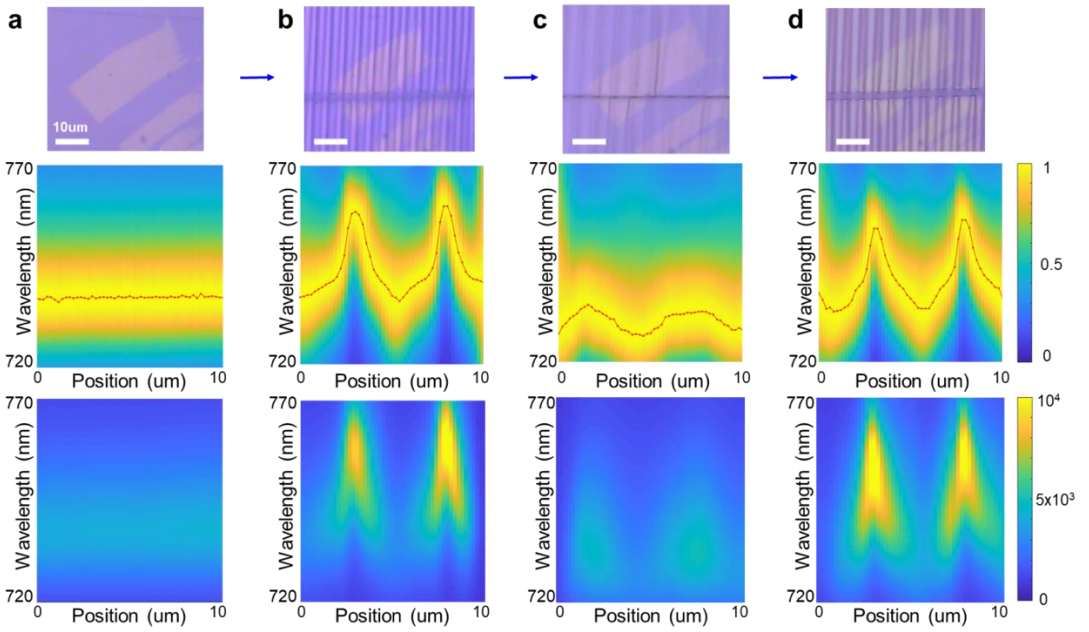

Fig. 6. Mechanically reconfigurable strain control of conformally wrinkled WSe_2. a, Flat WSe_2 with prestrain unreleased. **b,** Initial wrinkle structure after the prestrain released. **c,** Restretched state where external strain is about 90% of prestrain. **d,** Releasing external strain again to form wrinkle structure. The normalized PL line map reveals strain modulation as the wrinkle structure restretched and released again. The absolute PL line map shows PL intensification at apex due to strain-induced exciton effect.

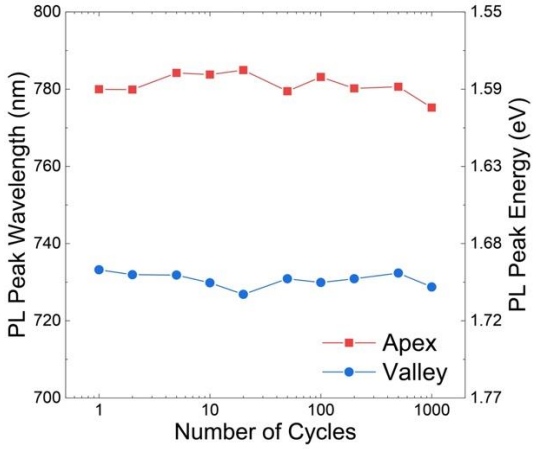

Fig. 7. Cyclic measurement of mechanical reconfigurability. PL peak wavelength (left y-axis) and corresponding peak energy (right y-axis) at apex (red) and valley (blue) were recorded over 1000 cycles of restretching (50% of initial prestrain) and releasing processes. Approximately 92% of initial local strain maintained after 1000 cycles.

Strain-induced modulation of exciton dynamics

To investigate the effect of local strain on exciton decay dynamics, we measured time-resolved PL (TRPL) spectra. Fig. 8 shows TRPL spectra from the flat WSe_2 and the wrinkled WSe_2 at apex and valley regions, respectively. Compared to the exciton decay on the flat WSe_2, exciton decay at the wrinkle apex significantly slowed, while exciton decay at the valley was facilitated. The longest lifetime components for flat WSe_2 and wrinkled WSe_2 at apex and valley were estimated to be 2.96, 8.54, and 1.27 ns, respectively. Interestingly, uniform tensile strain is known to cause faster exciton decay due to weak phonon-exciton coupling and destabilized Q-valley excitons in WSe_2[39]. We corroborated faster PL decay from WSe_2 under homogeneous tensile strain via two-point bending method (Fig. 9). These results imply that localized, heterogeneous strain greatly changes exciton decay dynamics and accurately modeling exciton decay under non-uniform strain requires taking both recombination and motion (i.e., diffusion and drift) of excitons into account in relation to strain gradient.

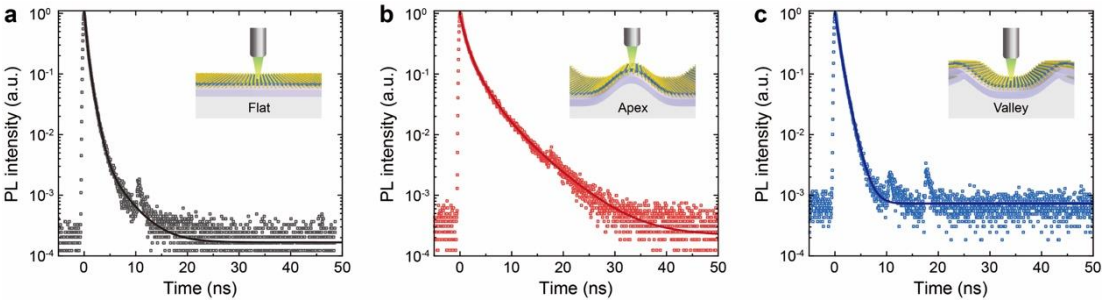

Fig. 8. Analyzing exciton decay behavior of flat and wrinkled WSe_2 depending on the localized strain. a, TRPL measured from flat WSe_2. **b-c,** TRPL measured from wrinkled WSe_2 at apex (**b**) and valley (**c**).

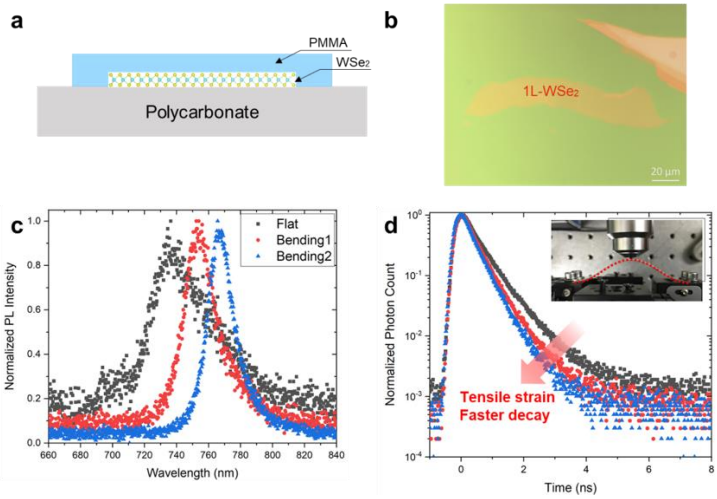

Fig. 9. Spatially homogeneous strain and time-resolved PL decay. a, Bending sample prepared by wet transfer of PMMA-supported WSe_2 on hydrophilic-treated polycarbonate (PC) substrate. **b,** Optical microscope image of monolayer WSe_2 on PC. **c,** PL shift as WSe_2 is bent. **d,** Time-resolved PL curve with different bending tensile strain with inset figure showing bending curvature.

To explain the trend of PL decay under heterogeneous local strain, we employed a spatiotemporal exciton continuity equation as shown in eqns (1) and (2). To solve the continuity equation, we consider the funneling of bright excitons (i.e., electron and hole both located at K-valley in the momentum space) through bandgap energy gradient (Fig. 10a). Because of significant modulation of conduction band minimum (CBM) by applied strain, bright excitons excited at valley of wrinkle are funneled to apex where excitons can possess the lowest potential energy[48]. The greater outward flux of excitons generated at valley leads to a reduced probability of observing exciton recombination at the excitation point, which explains the faster decrease of exciton density in TRPL measurement (Fig. 8c). However, for more quantitative fitting of decay curves, we need to take strain-dependent dark excitons into account in the continuity equation. Fig. 10b demonstrates how momentum-forbidden intervalley dark exciton affects exciton dynamics under local strain. Specifically, tensile strain shifts K-valley CBM closer to valence band (i.e., smaller bandgap) and Q-valley CBM away from valence band. For this reason, probability of phonon-assisted transition between bright state (KK) and momentum-forbidden state (KQ) varies by local strain, resulting in transition from KK to KQ excitons under compressive strain (valley) and transition from KQ to KK excitons under tensile strain (apex), thereby enhanced inflow of excitons to apex[49]. Furthermore, bright KK excitons can obtain additional drift momentum during exciton funneling, which delays or prohibits radiative decay of bright excitons[42,50]. In contrast, spin-forbidden dark excitons are expected to have negligible influence on strain-induced exciton dynamics because strain does not modulate energy difference between the spin-forbidden states and the bright states[49].

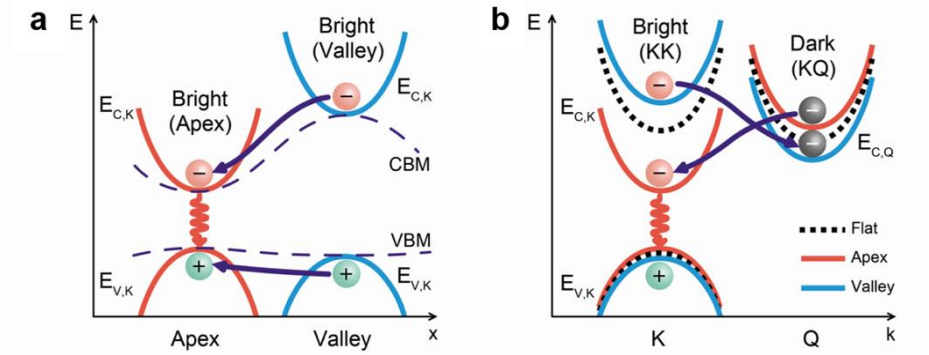

Fig 10. a, Schematic illustration of funneling of bright excitons from valley to apex owing to strain-induced energy gradient in real space. CBM and VBM indicate conduction band minimum and valence band maximum, respectively. **b**, Schematic of generation of dark exciton and its conversion to bright exciton at apex owing to lower exciton energy at apex due to tensile strain.

Taking the aforementioned effects into account and using physical parameters from literature and experimental conditions, we conducted numerical fitting of the continuity equation to the exciton decay curves (Fig. 11). A good agreement between the measured TRPL data and simulated fitting curves was observed in three different geometries (i.e., flat, wrinkle apex and valley), only when both bright and dark excitons were considered in the continuity equation. This indicates that the prolonged decay time at apex is attributed to the confinement of bright exciton in the local potential trap and preferential dark-to-bright conversion due to the improved stability of bright exciton at apex.

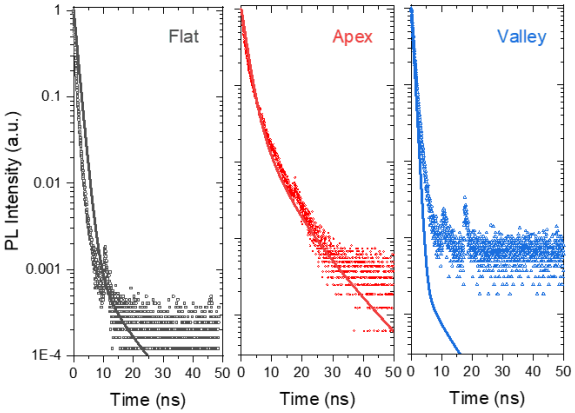

Fig. 11. Experimental and simulated TRPL from flat and wrinkled WSe_2. Experimental TRPL curves are denoted as dots and simulated decay curves are the bold line based on our exciton continuity equation.

Demonstration of exciton funneling via pump-probe PL measurement

In addition to the evidence of exciton funneling offered by delayed exciton decay, we performed steady-state pump-probe measurements to more conclusively demonstrate exciton funneling, as shown in bulk indirect excitons[32,33] and 2D interlayer excitons[36,51,52]. We used a pump-probe PL measurement setup that consisted of two sets of 2D galvo scanning systems allowing individual control of the pump and probe positions. While the pump laser was fixed at a specific position, reflection or fluorescence signals were collected over the (different) area of interest. The intensity profiles of the excitation laser exhibited the submicron-sized isotropic spots with a full-width at half maximum (FWHM) of ~0.5 μm (second rows in Fig. 12a-c). We then measured the emission profiles from the flat and wrinkled WSe_2 (third rows in Fig. 12a-c). While isotropic emission was observed on unstrained flat WSe_2, excitation at the apex of a wrinkle led to an elongated emission shape along the wrinkle apex. More importantly, valley pumping revealed remarkable PL emission at adjacent apexes. For comparison with the experimental emission features, we simulated the emission maps using parameters obtained from the TRPL curve fitting (fourth rows in Fig. 12a-c). The simulation results agreed very well with our measurements. These results reveal several features of exciton funneling. First, a radial diffusion occurred in the unstrained flat WSe_2 without directional drift. Second, excitons have lower potential energy at apex than the surrounding regions. Third, the exciton funneling was clearly observed during the valley-pumping, in which the potential energy gradient caused excitons generated at valley to drift toward apex and then recombine radiatively.

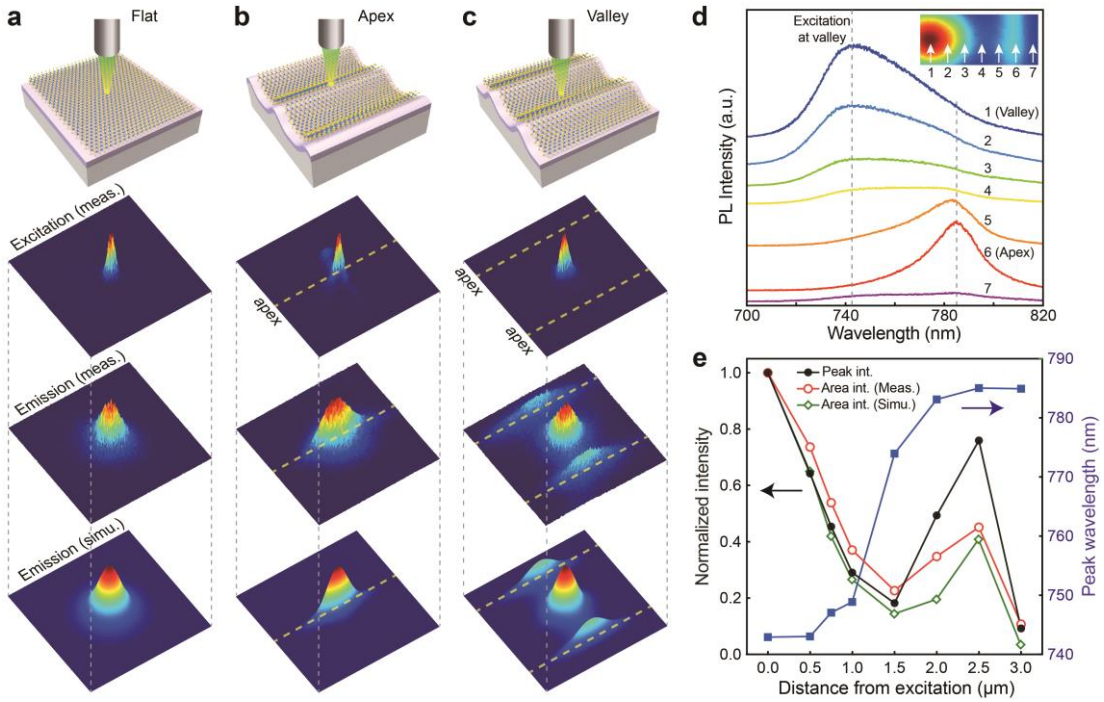

Fig. 12. Pump-probe characterization of exciton funneling under local strain gradient. a-c, Schematic of excitation points (top), measured excitation maps (second row), measured emission maps (third row), and simulated emission maps (bottom), from flat WSe_2 (**a**) and wrinkled WSe_2 excited at apex (**b**) and valley (**c**). The size of the excitation/emission maps is 8 x 8 μm^2. **d,** Measured PL spectra of wrinkled WSe_2 with excitation fixed at valley and emission detected from valley to adjacent apex. The distance from 1 (valley) to 7 is 3 μm with 6 being apex, and the spacing between consecutive numbers is 0.5 μm. **e,** Emission characteristics of funneling excitons in terms of measured PL peak intensity (black), measured fluorescence (area integrated PL; red), simulated fluorescence (green), and measured PL peak wavelength (right y-axis; blue).

We further investigated the efficiency of exciton funneling by measuring the sequential PL spectra from valley to one of the nearest apexes while fixing the excitation at the valley (Fig. 12d). As the probe position away from valley moved toward apex, gradual PL red-shift was observed. PL emission intensity decreased when the distance from the excitation was <1.5 μm, but increased when probing near apex (from 1.5 to 2.5 μm). These measured emission characteristics were summarized in Fig. 12e, together with simulated results. We observe several key features as follows. First, the measurement exhibited ~45% of relative fluorescence intensity and ~76% of relative PL peak intensity at 2.5 μm apart from excitation spot, which quantitatively agrees with relative fluorescence intensity obtained by simulation (~41%). Second, the relative emission intensity we measured from the intralayer excitons in strained monolayer WSe_2 was more than an order of magnitude higher than that from the interlayer excitons electrically drifted in 2D vertical heterostructure (~3% of relative PL emission intensity at 2.5 μm apart from excited point)[51]. Third, the observed funneling length (d) is comparable to values reported for strained MoS_2 energy harvesters (d ~ 3 μm at T = 270 K)[48]. If a similar estimation procedure is applied to our WSe_2 system, the calculation shows an exciton funneling length of 6.2 μm, which is comparable to our experimental value. Therefore, our measurement and simulation results suggest that strain-induced exciton funneling can be an efficient and predictable approach for exciton transport despite relatively short lifetime of intralayer excitons. Furthermore, the funneled exciton are measured far from the excited hot lattice, implying they are thermally relaxed cold excitons, suitable for studying many-body interactions such as Fermi liquids[34] or Bose-Einstein condensates (BEC)[32–36].

Modulation of exciton funneling in different funneling length and local strain

To investigate programmable exciton funneling, we demonstrate modulation of exciton funneling in different funneling length and strain. Fig. 13a shows top-view pump-probe emission maps with varying position of the pumping spot and strain distribution. First, we changed pumping position

sequentially from one apex to the adjacent apex and measured excitation/emission PL maps (Fig. 13a (i)-(iii) and Fig. 14). It manifests that pumping aside valley led to preferential exciton funneling toward the nearest apex and suppression of funneling to the second nearest apex in contrast to symmetric funneling in the case of pumping at the valley. In the case that the adjacent apexes have different degree of strain, the exciton distribution became also asymmetric (Fig. 13a (iv)), revealing preferential funneling toward apex under higher local strain. In contrast, neither exciton funneling from valley to apex nor exciton trapping along apex was observed from weakly strained WSe_2 (ε= 0.8%) despite the similar wrinkle geometry (Fig. 13a (v) and Fig. 14). In addition, the shorter funneling length (~1.5 μm) led to the similar level of PL intensity by funneled excitons at the apex compared to the PL intensity at excited valley (Fig. 14). We then plot the measured fluorescence (i.e., area-integrated PL intensity) of funneled exciton relative to fluorescence at pumping position as functions of funneling length and strain (Fig. 13b). The maximum funneling length in our measurement was about 2.9 μm with ~42% of relative fluorescence, and the maximum relative fluorescence was ~105% with 1.5 μm of funneling length. Taken together, all these results are supportive of our measurements in Fig. 12, indicating that the observed exciton funneling is attributed to local strain-induced bandgap modulation rather than out-of-plane structure.

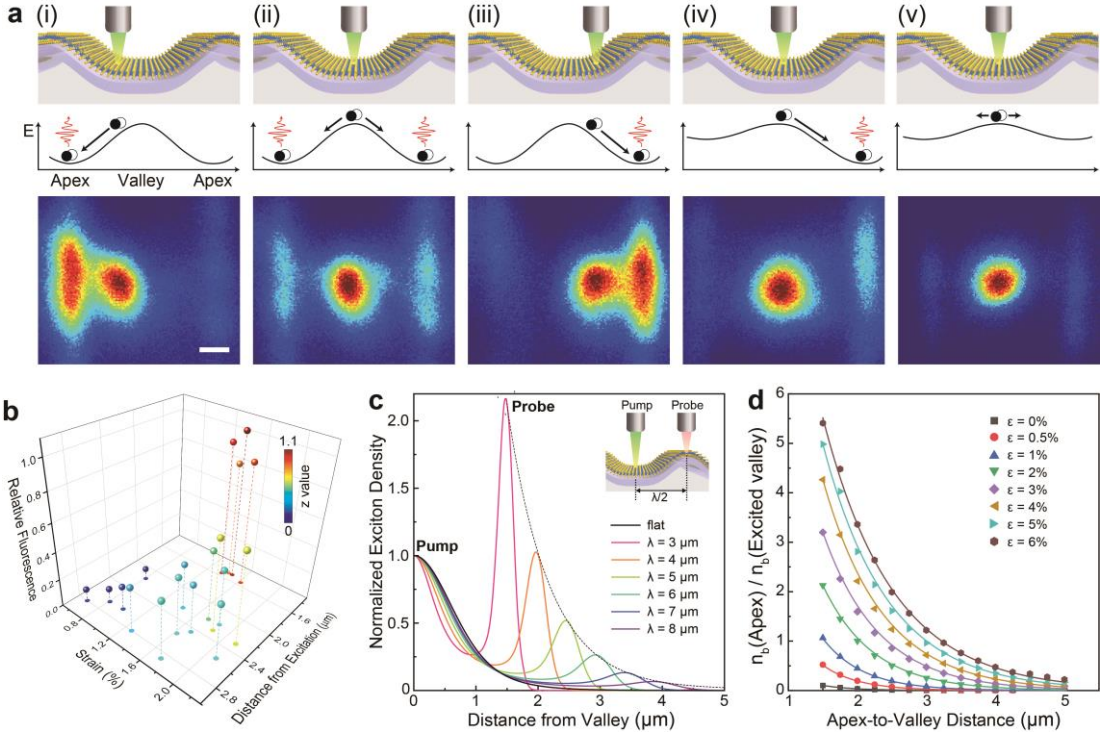

Fig. 13. Exciton funneling in different funneling length and local strain. a, Pump-probe measurements of wrinkled WSe_2 with different pumping position and local strain distribution. (i)-(iii) maps were measured in a same sample with varying the pumping spots. The asymmetric strain in (iv) was 0.63% (left apex) and 1.28% (right apex), while weak strain in (v) was 0.81% on both side apexes. Scale bar, 1 μm. **b,** Measured relative fluorescence of exciton funneled to apex with respect to funneling length and local strain. **c,** Simulated exciton distribution normalized by exciton density at pumping position (valley). The dotted line presents exponential fitting of exciton density at half of wavelengths (apex). **d,** Simulation of funneled exciton density n_b at apex relative to exciton density at excited valley as functions of distance (half of wrinkle wavelength) and applied strain ε.

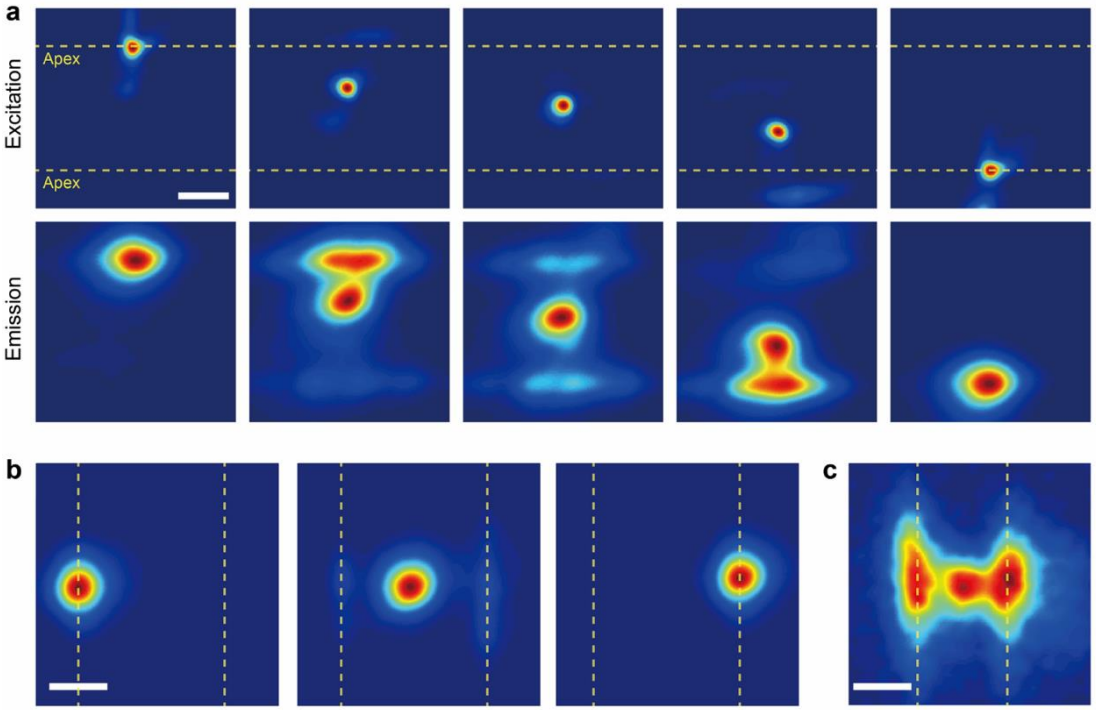

Fig. 14. Pump-probe PL maps as a function of pumping position. a, Measurements of sequential excitation from one apex to the adjacent apex (top) and corresponding emission maps (bottom). **b,** PL emission map of weakly strained WSe_2 (ε= 0.8%) with excitation point fixed at the left apex (left), the center valley (middle), and the right apex (right), showing less apparent funneling effect. **c,** PL emission map of WSe_2 with shorter wrinkle wavelength ($\lambda_{wrinkle}$ = 3.1 μm), showing the similar level of PL intensity by funneled excitons at the apex compared to the PL intensity at excited valley. Scale bars, 2 μm. The pump-probe excitation/emission maps were image processed by 2D Gaussian filtering in MATLAB to compensate the background noise signal, while the raw images in Fig. 13a result in the same trend.

We carried out simulation studies of exciton funneling in terms of funneling length and strain beyond our experimental observations. Fig. 13c shows simulated exciton distribution as a function of wrinkle wavelength. As wrinkle wavelength decreases, we observe that the exciton distribution becomes narrower near the pumping position and exciton density exponentially increased at apex. We also calculated relative density of funneled excitons at the apex with respect to strain (Fig. 13d). It shows that higher strain gradient owing to higher applied strain or shorter funneling length significantly improves funneling efficiency (Fig. 15). Further modification of wrinkle wavelength and strain (e.g., degree of local strain, asymmetry, biaxial strain) based on the theoretical prediction of exciton funneling dynamics will provide deeper insights for design of exciton-based straintronic circuits and devices[31].

Given that exciton funneling and confinement are crucial mechanism for realizing quantum emitters and quantum phase transition, we examine the feasibility of wrinkle-based exciton engineering by measuring PL emission at low temperature (T = 15 K) (Fig. 16). The fluorescence map revealed localized emissions along apex lines, which is consistent with the observation of quantum confinement of WSe_2 on silver nanowire[53]. The PL spectra measured at the apex shows sharp emission peaks as a result of exciton confinement induced by strain[7,8]. These results suggest the possibilities for mechanically reconfigurable quantum photonic applications.

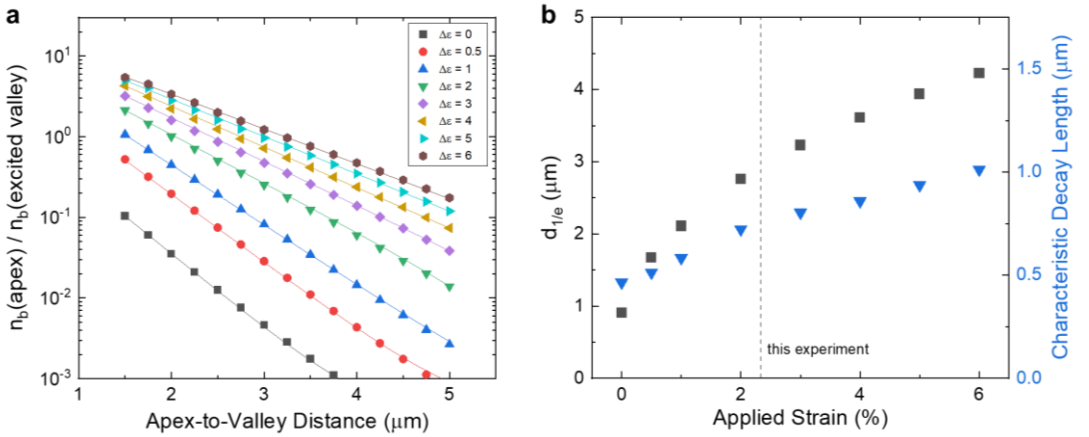

Fig. 15. Simulation of exciton funneling with varying applied strain and funneling length. a, Logarithmic plot of funneled exciton density at apex normalized by exciton density at excited valley. **b,** Modulation of $d_{1/e}$ (half of wrinkle wavelength at which density of funneled exciton at apex becomes 1 / e of exciton density at excited valley) and characteristic decay length (absolute value of inverse slope of **a**). The dotted line indicates our experimental strain value (2.4%).

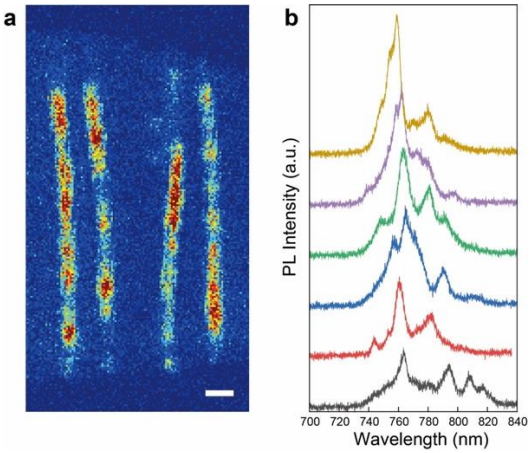

Fig. 16. Localized PL emission at low temperature (15 K). a, Fluorescence intensity map of wrinkled WSe_2, showing localized strong PL emission along the apex line. The scale bar is 5 μm. **b,** PL spectra of wrinkled WSe_2 at localized emission points in (a).

We have demonstrated uniaxial strain-induced exciton transport in steady-state pumping and probing experiments. On the other hand, straintronic logic device may require controllable exciton routing and transient exciton transport for ultrafast signal processing and logic operation. In this regard, we build a theoretical model of straintronic exciton router which is functional at GHz frequency signal processing on the basis of our experimental results and analysis on strained WSe_2. In this model, WSe_2 is conformally deformed as checkerboard-shape and exerted with biaxial tensile/compressive strain at the peak/valley of the structure (Fig. 17a-b). More specifically, the coordinate (0,0) and (1,1) in Fig. 17b indicate the valley under compressive strain and the peak under tensile strain, respectively, while (1,0) and (0,1) become local energy minima under reconfigurable stretching in y- or x-direction. The average strain gradient for both x- and y-direction is assumed to be 1.5% / 2.5 μm, with ratio of tensile and compressive strain same as the experimental value in uniaxial wrinkling. Modulation of exciton energy for biaxially strained state is determined by local strain (ε_{xx}, ε_{yy}) modulation of bandgap from neutral bandgap energy (1.65 eV). The distance between nearest peaks is 5 μm. We intend to control exciton transport direction as a function of reconfigurable local strain (Fig. 17c). For instance, stretching in x-direction causes elimination of x-direction local strain component (ε_{xx} = 0), resulting in exciton flux toward y-direction, denoted as (0,1) coordinate. The normalized exciton density at t = 0 ns and t = 2 ns is simulated and plotted in Fig. 17d and Fig. 17e-g, respectively. Excitation at the valley of the structure creates high energy excitons at t = 0 ns, which flow toward either (1,0), (0,1), or (1,1) direction. Specifically, biaxial local strain causes exciton drift

toward (1,1) direction. By changing local strain (e.g., stretching) in x- and y- directions we can induce exciton drift to (0,1) and (1,0) direction, respectively. The rate of exciton transport can be quantified by exponential time constant at the rising edge (τ_e) and 10/90 rise time ($\tau_{10/90}$), which revealed that straintronic device is functional at GHz frequencies (Fig. 18). We attribute the rapid exciton transport to reduced scattering of charge-neutral exciton with charged impurities and smooth energy gradient along the exciton transport path.

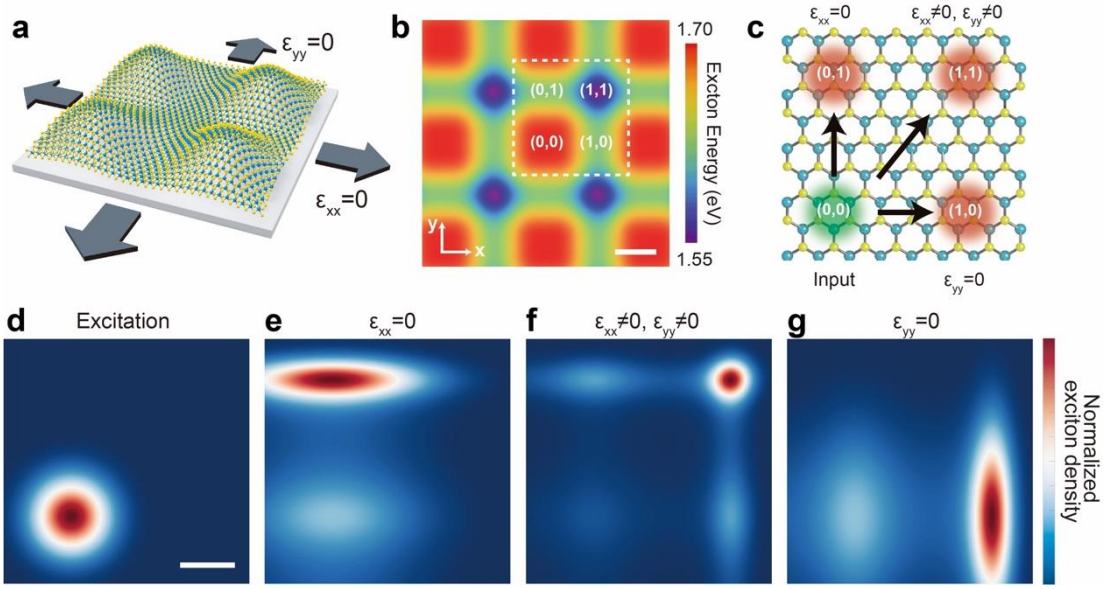

Fig. 17. Simulation of transient exciton router device. a, Schematic illustration of biaxially strained WSe_2 on elastomeric substrate. Stretching in x- or y- direction causes removal of local strain in the same direction (ε_{xx} = 0 or ε_{yy} = 0). **b,** Exciton energy distribution of biaxially strained WSe_2 device. Scale bar is 2 μm. **c,** Routing of exciton drift from valley (excitation) to energy minima in response to the reconfiguration of local strain. **d-g**, Simulated exciton density map of excited exciton (t = 0 ns) (**d**) and drifted excitons under different local strain at t = 2 ns. Stretching in x- (y-) direction causes annihilation of x- (y-) local strain component, resulting in y-direction exciton drift (**e**) or x-direction drift (**g**), respectively. On the other hand, biaxial local strain (no stretching) leads to exciton drift to (1,1) direction (**f**). Scale bar is 1 μm.

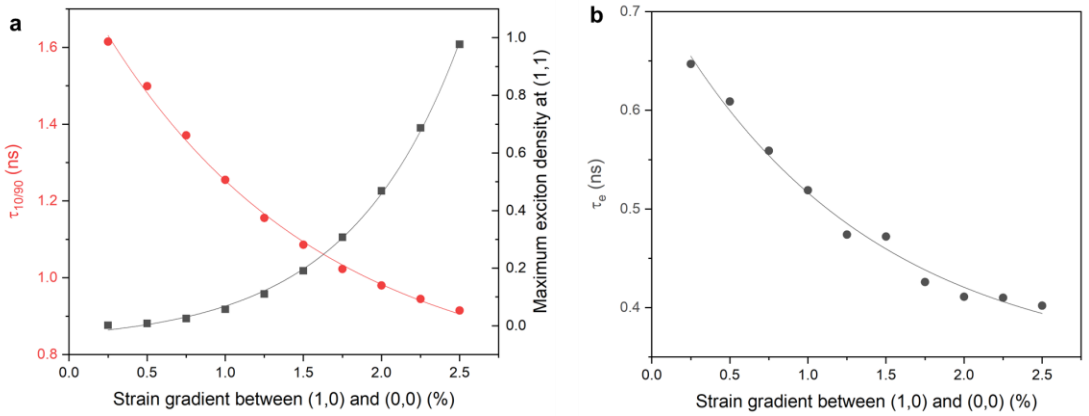

Fig. 18. Simulation of transient exciton drift of biaxially strained WSe_2 under different strain level. a, Summary of 10/90 rise time ($\tau_{10/90}$) and maximum exciton density at (1,1) position. Increasing strain enables faster exciton transport and greater signal obtained at the probing position. **b,** Exponential time constant at the rising edge (τ_e) as a function of strain gradient between (1,0) and (0,0).

Discussion

We have created conformally deformed soft wrinkle architecture which enables high local strain and optically-resolvable strain gradient on monolayer WSe_2. TRPL and pump-probe measurements manifested strain-dependent exciton decay and efficient exciton funneling with micrometer-scale funneling length. Our results not only open up opportunities for developing mechanically reconfigurable straintronic quantum devices, but also provide a platform for heterogeneous elastic strain engineering of diverse 2D materials for novel functionalities, including tunable magnetism, anisotropic thermal conductivity, and hydrogen evolution reaction, as a function of dynamically tunable strain gradient.

(2) Position and polarization controlled WSe_2 single photon emitters

Single photon source formed by gap strain

Fig. 19a shows a schematic illustration of our single photon source. The monolayer WSe_2 is placed on top of the dielectric rod structure with a nanogap that induces a local tensile strain. As shown in the schematic of the bandgap of WSe_2 (Fig. 19b), the nanogap can generate a spatially modulated artificial potential well through a tensile strain-induced perturbation of quantized energy states[54]. The excitons funnel into the manipulated states, implying position-controlled single photon emission. This strain-tuned emitter at the nanogap site dominates the photoluminescence (PL) intensity at low temperatures because of the efficient exciton funneling from the unstrained surrounding region to the lower localized energy level[55]. Furthermore, our structure for single photon emission allows control of its polarization in addition to its position. The saddle-shaped monolayer WSe_2 is formed at the nanogap site (Fig. 19c). The dominant direction of elongation is defined according to the nanogap size: the monolayer WSe_2 is elongated along the x-axis (y-axis) if the nanogap is relatively narrow (wide). The exciton oscillation occurs along the elongation axis.

To experimentally demonstrate the array of single photon emitters, we first fabricated Si_3N_4 rod structures with different gaps (d) and widths (w) on an SiO_2/Si substrate using electron-beam lithography and reactive ion etching. Fig 19d shows a scanning electron microscope (SEM) image of the fabricated Si_3N_4 rod structures. The value of d gradually changed from 60 nm (upper region) to 140 nm (lower region), whereas the value of w changed from 90 nm (left region) to 200 nm (right region). Different structural parameters of the nanogap can lead to different strains being applied to the monolayer WSe_2 placed on the rod. Next, monolayer WSe_2 flakes were transferred to the rod structures using the polydimethylsiloxane (PDMS) stamping method[56,57]. As shown in an optical microscope image of the finished sample (Fig. 19e), the monolayer WSe_2 flakes were successfully placed on the Si_3N_4 rod structures.

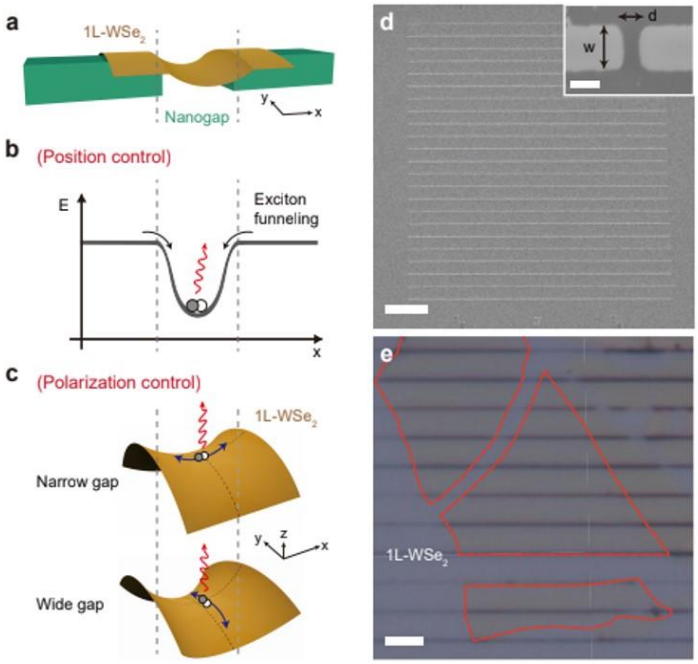

Fig. 19. Single photon source formed by gap strain. a, Schematic of a single photon source

consisting of monolayer WSe_2 and the dielectric rod structure with a nanogap. **b,** Schematic energy bandgap diagram along the x-axis in **a**. The bandgap of WSe_2 is engineered by the strain at the nanogap site and a potential well is formed. Optically generated excitons funnel into the potential well and recombine for localized emission. **c,** Schematics of the deformed monolayer WSe_2 due to the nanogap. The saddle-shaped deformation occurs along the x-axis (y-axis) for the narrow (wide) nanogap. The exciton oscillation is aligned with the elongation direction. **d,** SEM image of the fabricated Si_3N_4 rod structure array with nanogaps. The thickness of the Si_3N_4 layer was 150 nm. Scale bar, 10 μm. The inset shows a magnified SEM image of a nanogap (gap: *d*; width: *w*). Scale bar, 100 nm. **e,** Optical microscope image captured after the monolayer WSe_2 flakes were transferred onto the Si_3N_4 rod structures. The boundary of the monolayer WSe_2 is indicated by red dashed lines. Scale bar, 5 μm.

Measurement of single photon emission

A two-dimensional confocal PL intensity map was generated to find single photon emitters in the monolayer WSe_2 on the rods with nanogaps. A high-resolution fast raster scan was performed using a continuous-wave pump laser with a wavelength of 532 nm and two scanning galvo mirrors. The light emission from the monolayer WSe_2 was collected by objective lens and sent to a monochromator/charge-coupled device (CCD) or avalanche photodiodes via optical fibers. Additionally, a Hanbury Brown and Twiss (HBT) interferometer setup was constructed for the measurement of the second-order correlation. The temperature of the sample was varied from 4 K to room temperature.

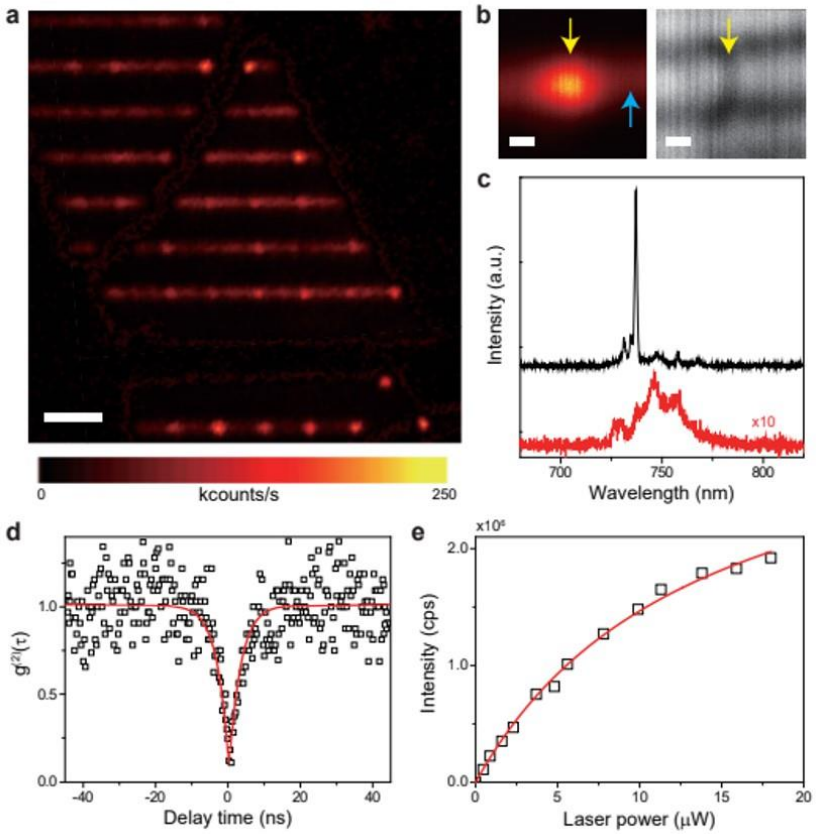

Fig. 20. Measurement of single photon emission. a, Measured PL intensity map for the structure in Fig. 19e. Localized photon emissions were observed at the nanogap sites. The pump power was 7.8 μW. Scale bar, 5 μm. **b,** High-resolution raster scanning images of PL (left) and reflection (right) near the nanogap site. The yellow arrows were inserted for comparison of the positions of the emission spot and the nanogap. The pump power was 2.3 μW for PL imaging. Scale bars, 100 nm. **c,** PL spectra measured at the positions of the yellow and blue arrows in the PL image of **b** (black and red curves, respectively). **d,** Measured photon correlation function $g^{(2)}$ of the highest peak (at 737.19 nm) in the black curve of **c**. A 10 nm-wide spectral filter was used for the measurement. The fitted red curve

indicates photon anti-bunching behavior with $g^{(2)}(0) = 0.108 \pm 0.041$. **e,** Integrated PL intensity as a function of the pump laser power. A 10-nm-wide spectral filter was used for the measurement. The fitted red curve indicates a saturation pump power of 13.7 μW and a saturation emission intensity of 1.47×10^6 count/s.

Figure 20a shows the measured PL intensity map of the strained monolayer WSe_2 at 4 K. Bright spots were observed at most of the nanogap sites of the Si_3N_4 rod structures, which exhibited PL intensities >10 times stronger than those of the surrounding areas with no gaps. To clarify the emitting positions, we obtained the high-resolution image of a single emission spot (Fig. 20b, left) and compared it with a reflection image of the rod structure (Fig. 20b, right). The positions of the bright spot and nanogap agreed very well; thus, the localized emission originated from the monolayer WSe_2 strained by the nanogap. Additionally, the PL spectra were measured at and near the nanogap (Fig. 20c). The spectrum measured at the nanogap site (yellow arrow in Fig. 20b) exhibited a strong emission peak at 737.19 nm with a sub-nanometer linewidth (<0.7 nm), whereas the measured PL spectrum was broad and weak for the rod with no gap (blue arrow in Fig. 20b). We note that the submicron-sized localized emission spot (~200 nm in size) and significant PL enhancement at the nanogap site were due to the exciton confinement resulting from the funneling effect[55].

Next, to verify the single photon feature of the emission, we measured the second-order correlation function $g^{(2)}(\tau)$ of a strong emission peak using the HBT setup. In the PL spectrum of Fig. 20c, a narrow spectral window was opened to select the sharp peak at 737.19 nm using a bandpass filter with a bandwidth of 10 nm. $g^{(2)}(\tau)$ was measured (dots in Fig. 20d) and fit with a three-level model (red line in Fig. 20d). The value of $g^{(2)}(0)$ was 0.108 ± 0.041, which indicates photon anti-bunching. More $g^{(2)}(0)$ values were measured from 0.045 ± 0.030 to 0.133 ± 0.044 at other nanogap sites (Fig. 21). Additionally, we measured the integrated PL intensity of the emission as a function of the pump power (Fig. 20e). Intensity saturation was observed, with a fitted saturation power of 13.7 μW and an integrated intensity of 1.47×10^6 counts/s at the saturation power.

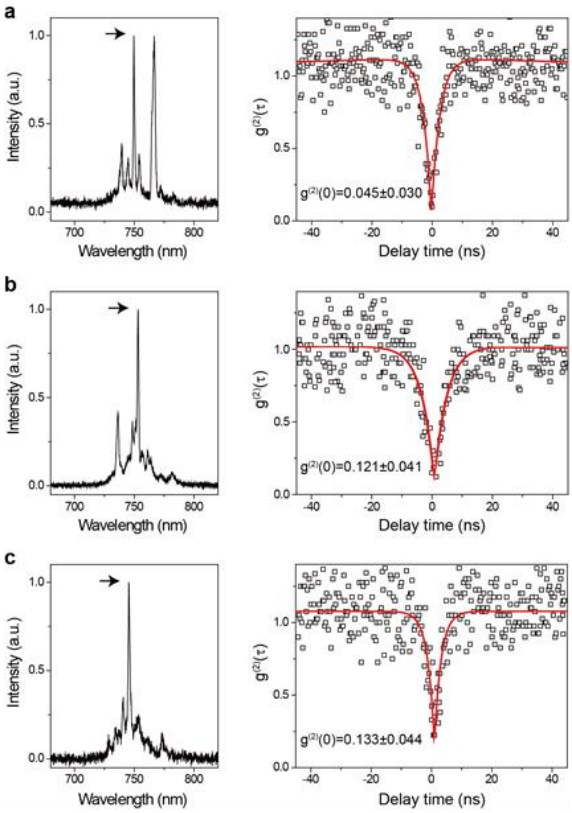

Fig. 21. Single photon properties of three different emitters. Measured PL spectra (**a-c**, left panels) and photon correlation functions $g^{(2)}$ (**a-c**, right panels) from three emitters at 4 K. Each $g^{(2)}$ was measured at the peak indicated by the arrow in the corresponding left panel: the peak wavelengths were (**a**) 749.61 nm, (**b**) 753.23 nm, and (**c**) 745.47 nm. Then, we obtained the $g^{(2)}(0)$ values: (**a**) 0.045

± 0.030, (**b**) 0.121 ± 0.041, and (**c**) 0.133 ± 0.044.

Temperature-dependent PL measurement and strain estimation

We characterized other key properties of the single photon emission at the nanogap sites. First, temperature-dependent PL spectra were measured while the sample temperature was varied from 4 to 20 K (Fig. 22a). The intensities and numbers of peaks decreased with the increasing temperature. To investigate the temperature dependence of the peak indicating photon anti-bunching, we plotted the intensity and linewidth of the highest peak at a wavelength of 758 nm as a function of the temperature (Fig. 22b). Above 20 K, the peak intensity decreased and the spectral linewidth increased significantly. This temperature-dependent behavior of single photon emission implies that the binding energy of the localized excitons at the nanogap site was lower than the thermal energy ($E_T = k_bT$) above the critical temperature of 20 K.

Next, we examined the strains introduced by the nanogap, by measuring the PL spectrum at room temperature (Fig. 23a). The wavelength of light emission at the nanogap site was redshifted by ~6–8 nm versus background because of the nanogap site-induced reduction of the bandgap of WSe_2[39,47,58]. The bandgap reduction was between 12.7 to 17.9 meV, which corresponds to an applied tensile strain between 0.26% and 0.36% (Fig. 23b)[39,47]. A strain of 0.16% was applied to the Si_3N_4 rod structure with no gap. The strain difference between the nanogap and the surroundings led to the formation of a potential well, giving rise to the funneling effect (see Fig. 19b)[55], when the thermal fluctuation was less than the potential well. We believe that this is the first observation to confirm that a small strain of ~0.2% can generate a potential well of sufficient depth, resulting in single photon emission.

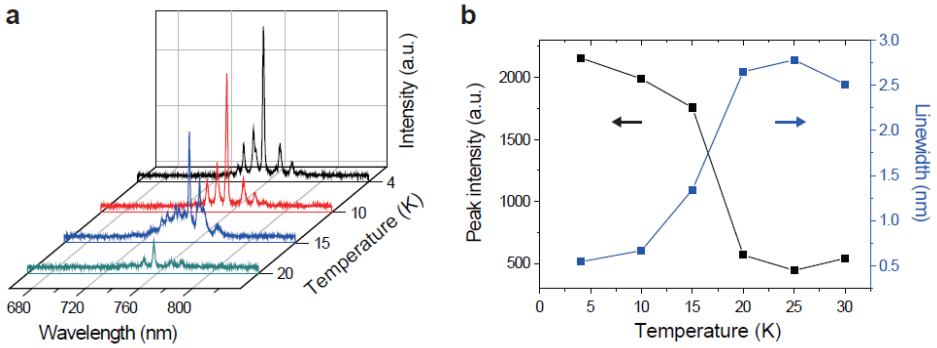

Fig. 22. Temperature-dependent properties. a, Measured PL spectra for the strained monolayer WSe_2 as functions of wavelength and temperature. The temperature varied from 4 to 20 K, and the pump power was 12.1 μW. **b,** Measured peak intensity (black) and spectral linewidth (blue) of the highest peak at a wavelength of 758.x nm in **a**, as a function of the temperature. Intensity suppression and linewidth broadening were observed above 20 K.

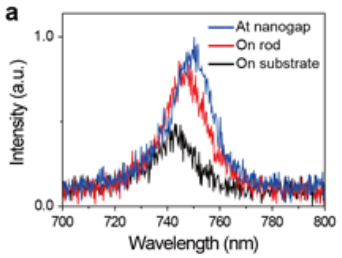

b

	λ (nm)	E (eV)	$\Delta E_{substrate}$ (meV)	ΔE_{rod} (meV)	Strain (%)
On substrate	742.59	1.6696	0 (ref)	n/	0
On rod	746.02	1.6619	7.7	0 (ref)	0.16
Nanogap (~70 nm)	750.27	1.6517	17.9	10.2	0.36
Nanogap (~90 nm)	748.36	1.6559	13.7	6.0	0.28
Nanogap (~110 nm)	747.91	1.6569	12.7	5.0	0.26
Nanogap (~130 nm)	749.04	1.6542	15.4	7.7	0.31

Fig. 23. Estimation of strains using PL shifts. **a,** Measured room-temperature PL spectra for three different regions: at the nanogap (blue), on the rod (red), and on the substrate (black). The center wavelengths were shifted by applied strains. **b,** Table presenting the measured center wavelengths (λ) and the corresponding estimated physical parameters for six different regions. E, $\Delta E_{substrate}$, and ΔE_{rod} represent the bandgap energy, the energy shift from the value on the substrate, and the energy shift from the value on the rod, respectively. The strain was estimated using the pre-reported factor of the PL shift controlled by uniaxial strain[39,47]. We used a gauge value of –49 meV/%, which was extracted from the PL measurement at room temperature.

Polarization characteristics

We investigated the polarization of the single photon emission at nanogap sites. To this end, the polarization-resolved PL intensity maps were measured using a linear polarizer placed in front of the detector (Figs. 24a and b). The sample of Fig. 20a was examined first. Interestingly, each single photon source was polarized either along or across the axis of the Si_3N_4 rod structure, which correspond to the horizontal and vertical polarization directions, respectively. In particular, the horizontally polarized emission was observed in the upper region of the sample with relatively narrow nanogaps (Fig. 24a), whereas the vertically polarized emission was observed in the lower region of the sample with relatively wide nanogaps (Fig. 24b). Figure 24c shows the measured polarization from the single photon emitter marked by the white dashed circle in Fig. 24a. The nanogap size was 90 nm at this site. Indeed, linearly polarized emissions along the horizontal direction (0° or 180°) were dominantly observed: the degree of polarization at the strongest peak was 0.928. Additionally, we measured the polarization from the single photon emitter at a nanogap with a size of 110 nm (white dashed circle in Fig. 24b). The vertical polarization direction (90°) was dominantly observed, with a degree of polarization of 0.962 (Fig. 24d). The polarization distribution of the 26 single photon emitters was plotted with respect to the nanogap size (Fig. 24e). This graph clearly indicated that the polarization direction changed depending on whether the nanogap was larger or smaller than 90 nm. We note that the width of the rod structure did not affect the polarization state.

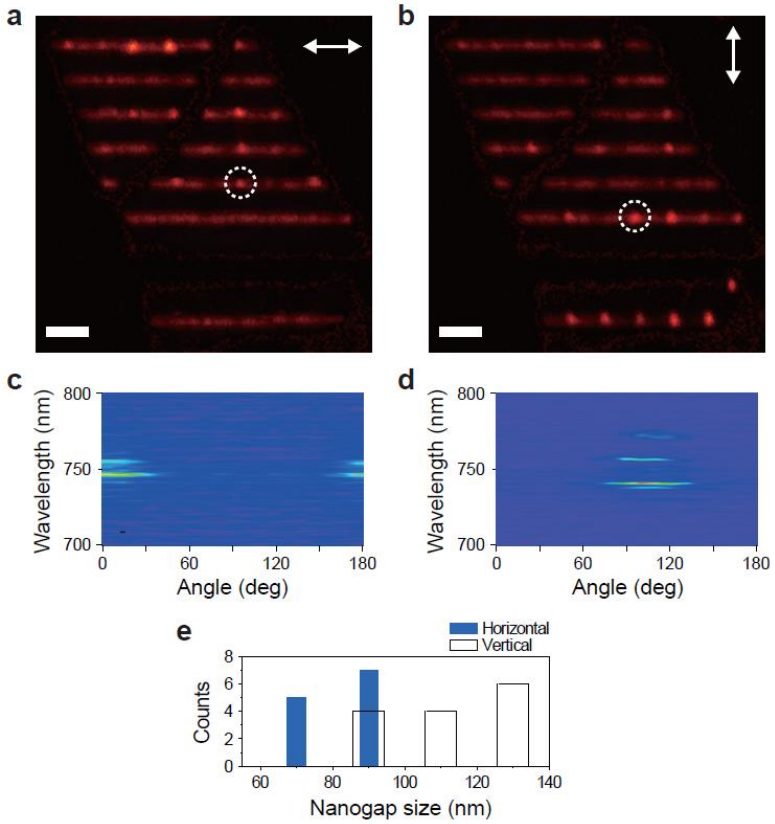

Fig. 24. Polarization-resolved measurements. a-b, PL intensity maps with horizontal (a) and vertical (b) polarization directions. Scale bars, 5 μm. **c-d,** Measured PL spectra as a function of the polarizer angle for the emitter positions indicated by the white dashed circles in **a** (c) and **b** (d). **e,** Number of emitters with horizontal (blue) and vertical (white) polarization directions for each nanogap size.

We measured polarization-resolved PL intensity maps for two additional samples (Fig. 25). Similar to Fig. 24, the polarization direction strongly depended on the nanogap size. When the nanogap was smaller or larger than a critical value, horizontal or vertical polarization was observed, respectively; the critical value of the nanogap size was 80 nm for Figs. 25a and c and 90 nm for Figs. 25b and d. Therefore, one can control the polarization of single photons by simply changing the size of the nanogap exerting strain on the monolayer WSe_2.

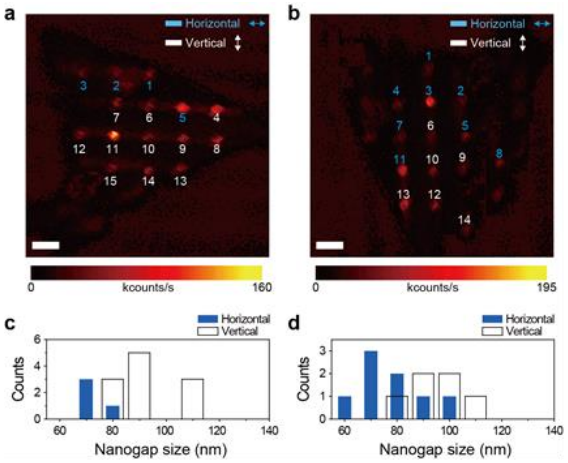

Fig. 25. Polarization-resolved measurements for two different samples. a-b, Polarization-resolved PL intensity maps of two samples with horizontal (blue) and vertical (white) polarization directions. There are 15 single photon emitters in **a** and 14 single photon emitters in **b**. Scale bars, 5 μm. **c-d,** Number of single photon emitters with horizontal (blue) and vertical (white) polarization directions as a function of the nanogap size. The graphs of **c** and **d** were plotted using the corresponding PL intensity maps of **a** and **b**, respectively.

The dependence of the polarization direction on the nanogap size is explained by the saddle-shaped anisotropic deformation of the monolayer WSe_2, as shown in Fig. 19c. Single photon emission was observed only when monolayer WSe_2 flakes were transferred onto the rod structures using an all-dry PDMS stamping method[54,56]. No single photon feature was observed when the conventional solution-based transfer method was used. The results of the experiment indicated that the pressure of the PDMS stamp could cause strain on the WSe_2 at the nanogap sites. To support this explanation, we simulated the morphology of the PDMS pressed onto the narrow (60 nm) or wide (140 nm) nanogap using the finite-element method (FEM). The simulation results indicated that two types of saddle-shaped deformation occurred in the PDMS, depending on the nanogap size (Figs. 3a and b). To investigate the deformation morphology, we examined the cross-sectional profiles along the x-axis (black dashed lines in Figs. 3a and b) and y-axis (white dashed lines in Figs. 3a and b). In case of the narrow nanogap (Fig. 3c), the y-axis deformation of the PDMS (red) was significantly larger than the x-axis deformation of the PDMS (black). However, for the wide nanogap, the x-axis deformation was dominant (Fig. 3d). Assuming that the morphology of the monolayer WSe_2 will follow that of the PDMS after the transfer process, our final WSe_2 morphology will exhibit anisotropic strains, resulting in gap-dependent exciton localization and two different polarization directions of single photons.

Integration of single photon emitters with optical cavities

To improve the performance of the single photon emitters, it is necessary to integrate the emitters with an optical cavity for enhancement of the Purcell factor[59]. Our single photon emitters in strained monolayer WSe_2 allows for adjustment of the polarization and position, making it easy to combine with nanocavities. For example, a one-dimensional photonic crystal cavity can be integrated with the Si_3N_4 rod structure by constructing an orthogonal structure (90° to each other) (Fig. 26a). The nanogap of the emitter and the no-air-hole defect region of the photonic crystal cavity are well matched in position; thus, the single photon emitter at the nanogap site can be coupled to the cavity. Indeed, we successfully fabricated the cavity-coupled single photon emitters by transferring the designed cavities onto strained monolayer WSe_2 using the transfer printing method (Fig. 26b)[60]. The top-view SEM image shows that the defect region of the photonic crystal nanobeam cavity was placed on top of the nanogap of the Si_3N_4 rod structure (inset of Fig. 26b).

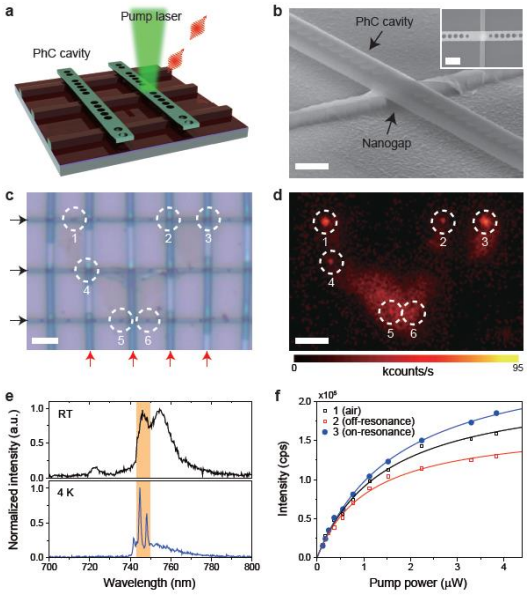

Fig. 26. Cavity-coupled single photon emitter. a, Schematic of the single photon emitters coupled to one-dimensional photonic crystal cavities. **b,** SEM image of a fabricated cavity-coupled single photon emitter. The photonic crystal cavity was transferred onto the nanogap. Scale bar, 500 nm. The inset shows the top-view SEM image. The photonic crystal cavity consists of three missing air holes in one-dimensional nanobeam structure with a lattice constant of 280 nm, a regular hole diameter of 195 nm, and a reduced hole diameter of 95 nm. The slab thickness and width of the nanobeam structure were 200 and 420 nm, respectively. Scale bar, 500 nm. **c,** Optical microscope image of the one-dimensional photonic crystal nanobeam cavity array transferred onto the Si_3N_4 rod structure array with nanogaps and strained monolayer WSe_2. The black and red arrows indicate the Si_3N_4 rod structures and photonic crystal structures, respectively. Scale bar, 3 μm. **d,** High-resolution raster scanning PL image of **c**. The pump power was 1.12 μW for PL imaging. Scale bar, 3 μm. **e,** Measured PL spectra of Emitter 3 at room temperature (top) and at 4 K (bottom). The cavity mode peak was observed at 746.1 nm (orange box, top). **f** Integrated PL intensity for Emitters 1 (black), 2 (red) and 3 (blue) as a function of the pump laser power. The fitted curves indicate saturation pump powers of 1.45 (black), 1.11 (red) and 1.74 μW (blue), and saturation emission intensities of 2.22×10^5 (black), 1.70×10^5 (red) and 2.67×10^5 count/s (blue).

We transferred the one-dimensional photonic crystal nanobeam cavity array onto the Si_3N_4 rod structure array with nanogaps and strained monolayer WSe_2, to make as many cavity-coupled single photon emitters as possible (Fig. 26c). The single photons emitted at the nanogaps were designed to be well-coupled to the photonic crystal nanobeam cavities: by fabricating narrow nanogaps with ~80 nm, the polarization direction of the emitted single photons is along the axis of the Si_3N_4 rod structure (i.e. perpendicular to the photonic crystal nanobeam cavity). Among six single photon emitters (Fig. 27a), three (Emitters 1, 5 and 6) were uncoupled and the other three (Emitters 2, 3 and 4) were coupled to photonic crystal nanobeam cavities (Fig. 26c). Figure 26d shows the measured PL intensity map of this sample at 4 K. Emitter 3 was observed to be brighter than the other emitters.

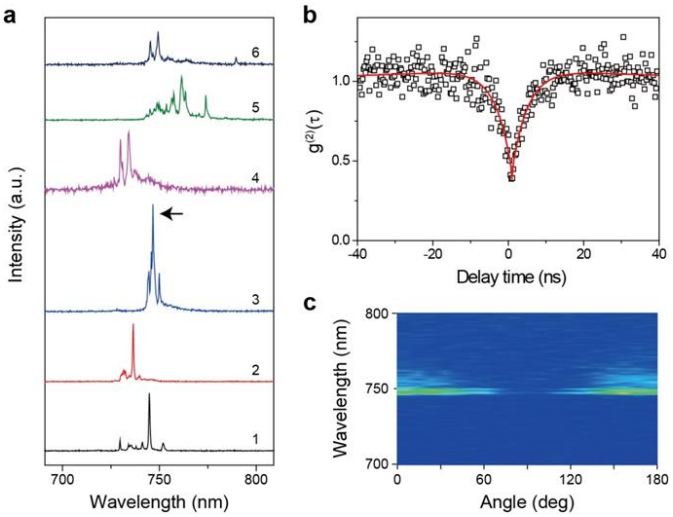

Fig. 27. Emission properties of cavity-coupled single photon sources. a Measured PL spectra at 4 K at the positions indicated by the white dashed circles in Fig. 26c and d. **b** Measured photon correlation function $g^{(2)}$ at the peak indicated by the black arrow in **a**. We obtained the $g^{(2)}(0)$ value of 0.384 ± 0.095. **c** Measured PL spectrum as a function of the polarizer angle for Emitter 3 in Fig. 26c and d.

To further investigate the optical properties of Emitter 3, we first measured room-temperature PL, which shows only resonance feature of the photonic crystal nanobeam cavity. The cavity mode peak was observed at 746.1 nm, showing Q factor of ~170 (orange box in the top panel, Fig. 26e). The comparison between the PL spectra measured at room temperature and 4 K shows that this single photon emitter is spectrally well-matched to the cavity mode (Fig. 26e). Emitter 3 also exhibited photon anti-bunching behavior (Fig. 27b) and linearly polarized direction along the Si_3N_4 rod structure, as expected (Fig. 27c). Notably, the saturation emission intensity quantitatively shows that Emitter 3 is brighter than the uncoupled emitter (Emitter 1) or off-resonance coupled emitter (Emitter 2), as a result of the on-resonance coupling of Emitter 3 with the photonic crystal nanobeam cavity (Fig. 26f). Thus, we note that this experiment will help facilitate the demonstration of a scalable and integrable single photon source array.

Discussion

In summary, we demonstrated deterministic control of both the position and polarization of single photon emitters in atomically thin WSe_2 placed on a nanogap array. Manipulation of the band structure by a local strain gradient generated a potential well at the nanogap site, and position-controlled single photon emission was subsequently achieved. Additionally, directional elongations of the potential well, which were tuned by changing the nanogap size, allowed polarization-controlled single photon emission. Moreover, single photons with a $g^{(2)}$ of ~0.1 were generated at 4–20 K. To take a full advantage of such deterministic control of the position and polarization of single photon emitters, we successfully integrated the emitters with one-dimensional photonic crystal nanobeam cavities. Therefore, we believe that our approach is a unique way to develop next-generation, deterministic, controllable single photon emitters based on TMDC materials, which outperform the present single photon sources with random occurrence and uncontrolled polarization properties.

Reference

1. H. K. Lo, M. Curty, and K. Tamaki: Secure quantum key distribution. *Nat. Photonics* **8**(8), 595 (2014).
2. C. Santori, D. Fattal, J. Vučković, G. S. Solomon, and Y. Yamamoto: Indistinguishable photons from a single-photon device. *Nature* **419**, 594 (2002).
3. P. Michler, A. Imamoğlu, M. D. Mason, P. J. Carson, G. F. Strouse, and S. K. Buratto: Quantum correlation among photons from a single quantum dot at room temperature. *Nature* **406**(6799), 968 (2000).

4. I. Aharonovich, D. Englund, and M. Toth: Solid-state single-photon emitters. *Nat. Photonics* **10**(10), 631 (2016).
5. T. T. Tran, C. Elbadawi, D. Totonjian, C. J. Lobo, G. Grosso, H. Moon, D. R. Englund, M. J. Ford, I. Aharonovich, and M. Toth: Robust multicolor single photon emission from point defects in hexagonal boron nitride. *ACS Nano* **10**, 7331 (2016).
6. G. Grosso, H. Moon, B. Lienhard, S. Ali, D. K. Efetov, M. M. Furchi, P. Jarillo-Herrero, M. J. Ford, I. Aharonovich, and D. Englund: Tunable and high-purity room temperature single-photon emission from atomic defects in hexagonal boron nitride. *Nat. Commun.* **8**, 705 (2017).
7. A. M. Berhane, K. Y. Jeong, Z. Bodrog, S. Fiedler, T. Schröder, N. V. Triviño, T. Palacios, A. Gali, M. Toth, D. Englund, and I. Aharonovich: Bright Room-Temperature Single-Photon Emission from Defects in Gallium Nitride. *Adv. Mater.* **29**, 1605092 (2017).
8. I. Lovchinsky, J. D. Sanchez-Yamagishi, E. K. Urbach, S. Choi, S. Fang, T. I. Andersen, K. Watanabe, T. Taniguchi, A. Bylinskii, E. Kaxiras, P. Kim, H. Park, and M. D. Lukin: Magnetic resonance spectroscopy of an atomically thin material using a single-spin qubit. *Science* **355**(6324), 503 (2017).
9. Y. Zhou, A. Rasmita, K. Li, Q. Xiong, I. Aharonovich, and W. B. Gao: Coherent control of a strongly driven silicon vacancy optical transition in diamond. *Nat. Commun.* **8**, 14451 (2017).
10. C. Zhang, S. Zhao, C. Jin, A. L. Koh, Y. Zhou, W. Xu, Q. Li, Q. Xiong, H. Peng, and Z. Liu: Direct growth of large-area graphene and boron nitride heterostructures by a co-segregation method. *Nat. Commun.* **6**, 6519 (2015).
11. I. Söllner, S. Mahmoodian, S. L. Hansen, L. Midolo, A. Javadi, G. Kiršanske, T. Pregnolato, H. El-Ella, E. H. Lee, J. D. Song, S. Stobbe, and P. Lodahl: Deterministic photon-emitter coupling in chiral photonic circuits. *Nat. Nanotechnol.* **10**(9), 775 (2015).
12. A. Badolato, K. Hennessy, M. Atatüre, J. Dreiser, E. Hu, P. M. Petroff, and A. Imamoğlu: Deterministic coupling of single quantum dots to single nanocavity modes. *Science* **308**(5725), 1158 (2005).
13. C. Schneider, M. Strauß, T. Sünner, A. Huggenberger, D. Wiener, S. Reitzenstein, M. Kamp, S. Höfling, and A. Forchel: Lithographic alignment to site-controlled quantum dots for device integration. *Appl. Phys. Lett.* **92**, 183101 (2008).
14. T. Schröder, M. E. Trusheim, M. Walsh, L. Li, J. Zheng, M. Schukraft, A. Sipahigil, R. E. Evans, D. D. Sukachev, C. T. Nguyen, J. L. Pacheco, R. M. Camacho, E. S. Bielejec, M. D. Lukin, and D. Englund: Scalable focused ion beam creation of nearly lifetime-limited single quantum emitters in diamond nanostructures. *Nat. Commun.* **8**, 15376 (2017).
15. T. Schröder, M. Walsh, J. Zheng, S. Mouradian, L. Li, G. Malladi, H. Bakhru, M. Lu, A. Stein, M. Heuck, and D. Englund: Scalable fabrication of coupled NV center - photonic crystal cavity systems by self-aligned N ion implantation. *Opt. Mater. Express* **7**(5), 1514 (2017).
16. Y. C. Chen, P. S. Salter, S. Knauer, L. Weng, A. C. Frangeskou, C. J. Stephen, S. N. Ishmael, P. R. Dolan, S. Johnson, B. L. Green, G. W. Morley, M. E. Newton, J. G. Rarity, M. J. Booth, and J. M. Smith: Laser writing of coherent colour centres in diamond. *Nat. Photonics* **11**(2), 77 (2017).
17. M. Koperski, K. Nogajewski, A. Arora, V. Cherkez, P. Mallet, J. Y. Veuillen, J. Marcus, P. Kossacki, and M. Potemski: Single photon emitters in exfoliated WSe2 structures. *Nat. Nanotechnol.* **10**(6), 503 (2015).
18. Y. M. He, G. Clark, J. R. Schaibley, Y. He, M. C. Chen, Y. J. Wei, X. Ding, Q. Zhang, W. Yao, X. Xu, C. Y. Lu, and J. W. Pan: Single quantum emitters in monolayer semiconductors. *Nat. Nanotechnol.* **10**(6), 497 (2015).
19. A. Srivastava, M. Sidler, A. V. Allain, D. S. Lembke, A. Kis, and A. Imamoglu: Optically active quantum dots in monolayer WSe 2. *Nat. Nanotechnol.* **10**(6), 491 (2015).
20. C. Palacios-Berraquero, D. M. Kara, A. R. P. Montblanch, M. Barbone, P. Latawiec, D. Yoon, A. K. Ott, M. Loncar, A. C. Ferrari, and M. Atatüre: Large-scale quantum-emitter arrays in atomically thin semiconductors. *Nat. Commun.* **8**, 15093 (2017).
21. G. D. Shepard, O. A. Ajayi, X. Li, X. Y. Zhu, J. Hone, and S. Strauf: Nanobubble induced formation of quantum emitters in monolayer semiconductors. *2D Mater.* **4**, 021019 (2017).
22. F. Peyskens, C. Chakraborty, M. Muneeb, D. Van Thourhout, and D. Englund: Integration of single photon emitters in 2D layered materials with a silicon nitride photonic chip. *Nat. Commun.* **10**(1), 1 (2019).
23. J. Kern, I. Niehues, P. Tonndorf, R. Schmidt, D. Wigger, R. Schneider, T. Stiehm, S. Michaelis

de Vasconcellos, D. E. Reiter, T. Kuhn, and R. Bratschitsch: Nanoscale Positioning of Single-Photon Emitters in Atomically Thin WSe2. *Adv. Mater.* **28**(33), 7101 (2016).
24. S. Yang, C. Wang, H. Sahin, H. Chen, Y. Li, S. S. Li, A. Suslu, F. M. Peeters, Q. Liu, J. Li, and S. Tongay: Tuning the optical, magnetic, and electrical properties of ReSe2 by nanoscale strain engineering. *Nano Lett.* **15**(3), 1660 (2015).
25. H. Li, A. W. Contryman, X. Qian, S. M. Ardakani, Y. Gong, X. Wang, J. M. Weisse, C. H. Lee, J. Zhao, P. M. Ajayan, J. Li, H. C. Manoharan, and X. Zheng: Optoelectronic crystal of artificial atoms in strain-textured molybdenum disulphide. *Nat. Commun.* **6**, 7381 (2015).
26. A. V. Tyurnina, D. A. Bandurin, E. Khestanova, V. G. Kravets, M. Koperski, F. Guinea, A. N. Grigorenko, A. K. Geim, and I. V. Grigorieva: Strained Bubbles in van der Waals Heterostructures as Local Emitters of Photoluminescence with Adjustable Wavelength. *ACS Photonics* **6**(2), 516 (2019).
27. J. Pető, G. Dobrik, G. Kukucska, P. Vancsó, A. A. Koós, J. Koltai, P. Nemes-Incze, C. Hwang, and L. Tapasztó: Moderate strain induced indirect bandgap and conduction electrons in MoS2 single layers. *npj 2D Mater. Appl.* **3**, 39 (2019).
28. A. Castellanos-Gomez, R. Roldán, E. Cappelluti, M. Buscema, F. Guinea, H. S. J. Van Der Zant, and G. A. Steele: Local strain engineering in atomically thin MoS2. *Nano Lett.* **13**(11), 5361 (2013).
29. K. P. Dhakal, S. Roy, H. Jang, X. Chen, W. S. Yun, H. Kim, J. Lee, J. Kim, and J. H. Ahn: Local Strain Induced Band Gap Modulation and Photoluminescence Enhancement of Multilayer Transition Metal Dichalcogenides. *Chem. Mater.* **29**(12), 5124 (2017).
30. D. F. Cordovilla Leon, Z. Li, S. W. Jang, C. H. Cheng, and P. B. Deotare: Exciton transport in strained monolayer WSe2. *Appl. Phys. Lett.* **113**, 252101 (2018).
31. A. A. Bukharaev, A. K. Zvezdin, A. P. Pyatakov, and Y. K. Fetisov: Straintronics: a new trend in micro- and nanoelectronics and material science. *Uspekhi Fiz. Nauk* **188**(12), 1288 (2018).
32. K. Yoshioka, E. Chae, and M. Kuwata-Gonokami: Transition to a Bose-Einstein condensate and relaxation explosion of excitons at sub-Kelvin temperatures. *Nat. Commun.* **2**, 328 (2011).
33. P. L. Gourley and J. P. Wolfe: Spatial condensation of strain-confined excitons and excitonic molecules into an electron-hole liquid in silicon. *Phys. Rev. Lett.* **40**(8), 526 (1978).
34. T. B. Arp, D. Pleskot, V. Aji, and N. M. Gabor: Electron–hole liquid in a van der Waals heterostructure photocell at room temperature. *Nat. Photonics* **13**, 245 (2019).
35. Z. Wang, D. A. Rhodes, K. Watanabe, T. Taniguchi, J. C. Hone, J. Shan, and K. F. Mak: Evidence of high-temperature exciton condensation in two-dimensional atomic double layers. *Nature* **574**(7776), 76 (2019).
36. D. Unuchek, A. Ciarrocchi, A. Avsar, Z. Sun, K. Watanabe, T. Taniguchi, and A. Kis: Valley-polarized exciton currents in a van der Waals heterostructure. *Nat. Nanotechnol.* **14**, 1104 (2019).
37. L. Yuan and L. Huang: Exciton dynamics and annihilation in WS2 2D semiconductors. *Nanoscale* **7**(16), 7402 (2015).
38. S. Mouri, Y. Miyauchi, M. Toh, W. Zhao, G. Eda, and K. Matsuda: Nonlinear photoluminescence in atomically thin layered WSe2 arising from diffusion-assisted exciton-exciton annihilation. *Phys. Rev. B - Condens. Matter Mater. Phys.* **90**, 155449 (2014).
39. I. Niehues, R. Schmidt, M. Drüppel, P. Marauhn, D. Christiansen, M. Selig, G. Berghäuser, D. Wigger, R. Schneider, L. Braasch, R. Koch, A. Castellanos-Gomez, T. Kuhn, A. Knorr, E. Malic, M. Rohlfing, S. Michaelis De Vasconcellos, and R. Bratschitsch: Strain Control of Exciton-Phonon Coupling in Atomically Thin Semiconductors. *Nano Lett.* **18**(3), 1751 (2018).
40. M. Hosseini, M. Elahi, M. Pourfath, and D. Esseni: Very large strain gauges based on single layer MoSe2 and WSe2 for sensing applications. *Appl. Phys. Lett.* **107**, 253503 (2015).
41. G. H. Peng, P. Y. Lo, W. H. Li, Y. C. Huang, Y. H. Chen, C. H. Lee, C. K. Yang, and S. J. Cheng: Distinctive Signatures of the Spin- and Momentum-Forbidden Dark Exciton States in the Photoluminescence of Strained WSe 2 Monolayers under Thermalization. *Nano Lett.* **19**(4), 2299 (2019).
42. C. D. Spataru, S. Ismail-Beigi, R. B. Capaz, and S. G. Louie: Theory and Ab initio calculation of radiative lifetime of excitons in semiconducting carbon nanotubes. *Phys. Rev. Lett.* **95**, 247402 (2005).
43. C. Robert, T. Amand, F. Cadiz, D. Lagarde, E. Courtade, M. Manca, T. Taniguchi, K. Watanabe, B. Urbaszek, and X. Marie: Fine structure and lifetime of dark excitons in transition metal dichalcogenide monolayers. *Phys. Rev. B* **96**, 155423 (2017).

44. T. Deilmann and K. S. Thygesen: Finite-momentum exciton landscape in mono- and bilayer transition metal dichalcogenides. *2D Mater.* **6**, 035003 (2019).
45. S. Deng, E. Gao, Z. Xu, and V. Berry: Adhesion Energy of MoS2 Thin Films on Silicon-Based Substrates Determined via the Attributes of a Single MoS2 Wrinkle. *ACS Appl. Mater. Interfaces* **9**(8), 7812 (2017).
46. C. J. Brennan, J. Nguyen, E. T. Yu, and N. Lu: Interface Adhesion between 2D Materials and Elastomers Measured by Buckle Delaminations. *Adv. Mater. Interfaces* **2**, 1500176 (2015).
47. R. Schmidt, I. Niehues, R. Schneider, M. Drüppel, T. Deilmann, M. Rohlfing, S. M. De Vasconcellos, A. Castellanos-Gomez, and R. Bratschitsch: Reversible uniaxial strain tuning in atomically thin WSe2. *2D Mater.* **3**, 021011 (2016).
48. J. Feng, X. Qian, C. W. Huang, and J. Li: Strain-engineered artificial atom as a broad-spectrum solar energy funnel. *Nat. Photonics* **6**(12), 866 (2012).
49. G.-H. Peng, P.-Y. Lo, W.-H. Li, Y.-C. Huang, Y.-H. Chen, C.-H. Lee, C.-K. Yang, and S.-J. Cheng: Distinctive Signatures of the Spin- and Momentum-Forbidden Dark Exciton States in the Photoluminescence of Strained WSe2 Monolayers under Thermalization. *Nano Lett.* **19**(4), 2299 (2019).
50. L. V. Butov, A. C. Gossard, and D. S. Chemla: Macroscopically ordered state in an exciton system. *Nature* **418**(6899), 751 (2002).
51. D. Unuchek, A. Ciarrocchi, A. Avsar, K. Watanabe, T. Taniguchi, and A. Kis: Room-temperature electrical control of exciton flux in a van der Waals heterostructure. *Nature* **560**(7718), 340 (2018).
52. L. A. Jauregui, A. Y. Joe, K. Pistunova, D. S. Wild, A. A. High, Y. Zhou, G. Scuri, K. de Greve, A. Sushko, C. H. Yu, T. Taniguchi, K. Watanabe, D. J. Needleman, M. D. Lukin, H. Park, and P. Kim: Electrical control of interlayer exciton dynamics in atomically thin heterostructures. *Science* **366**(6467), 870 (2019).
53. T. Cai, S. Dutta, S. Aghaeimeibodi, Z. Yang, S. Nah, J. T. Fourkas, and E. Waks: Coupling Emission from Single Localized Defects in Two-Dimensional Semiconductor to Surface Plasmon Polaritons. *Nano Lett.* **17**(11), 6564 (2017).
54. L. Linhart, M. Paur, V. Smejkal, J. Burgdörfer, T. Mueller, and F. Libisch: Localized Intervalley Defect Excitons as Single-Photon Emitters in WSe2. *Phys. Rev. Lett.* **123**(14), 146401 (2019).
55. H. Moon, G. Grosso, C. Chakraborty, C. Peng, T. Taniguchi, K. Watanabe, and D. Englund: Dynamic exciton funneling by local strain control in a monolayer semiconductor. *arXiv Prepr. arXiv* https://arxiv.org/abs/1906.10077 (2019).
56. A. Castellanos-Gomez, M. Buscema, R. Molenaar, V. Singh, L. Janssen, H. S. J. Van Der Zant, and G. A. Steele: Deterministic transfer of two-dimensional materials by all-dry viscoelastic stamping. *2D Mater.* **1**, 011002 (2014).
57. D. H. Tien, J. Y. Park, K. B. Kim, N. Lee, T. Choi, P. Kim, T. Taniguchi, K. Watanabe, and Y. Seo: Study of Graphene-based 2D-Heterostructure Device Fabricated by All-Dry Transfer Process. *ACS Appl. Mater. Interfaces* **8**(5), 3072 (2016).
58. S. B. Desai, G. Seol, J. S. Kang, H. Fang, C. Battaglia, R. Kapadia, J. W. Ager, J. Guo, and A. Javey: Strain-induced indirect to direct bandgap transition in multilayer WSe2. *Nano Lett.* **14**(8), 4592 (2014).
59. A. Badolato, K. Hennessy, M. Atatüre, J. Dreiser, E. Hu, P. M. Petroff, and A. Imamoğlu: Deterministic coupling of single quantum dots to single nanocavity modes. *Science* **308**(5725), 1158 (2005).
60. J. Lee, I. Karnadi, J. T. Kim, Y. H. Lee, and M. K. Kim: Printed nanolaser on silicon. *ACS Photonics* **4**(9), 2117 (2017).

List of Publications and Significant Collaborations that resulted from your AOARD supported project:

a) papers published in peer-reviewed journals,

1. J.-P. So, K.-Y. Jeong, J. M. Lee, K.-H. Kim, S.-J. Lee, W. Huh, H.-R. Kim, J.-H. Choi, J. M. Kim, Y. S. Kim, C.-H. Lee, S. Nam*, and H.-G. Park*, "Polarization Control of Deterministic Single-Photon Emitters in Monolayer WSe2," *Nano Letters* 21, 1546 (2021).
2. Kwang-Yong Jeong, Min-Soo Hwang, Jungkil Kim, Jin-Sung Park, Jung Min Lee, and Hong-Gyu Park*, "Recent progress in nanolaser technology," *Advanced Materials* 32, 202001996

(2020).
3. Jungkil Kim, Hoo-Cheol Lee, Ha-Reem Kim, Hosung Lee, Jung Min Lee, Kwang-Yong Jeong, and Hong-Gyu Park*, "Si nanowires with porous segments for photon-triggered transistors," *J. Phys. D: Appl. Phys.* 52, 373001 (2019).
4. Hoo-Cheol Lee, Soon-Jae Lee, Jungkil Kim, Kyoung-Ho Kim, Jin-Sung Park, Min-Soo Hwang, Jung Min Lee, Kwang-Yong Jeong*, and Hong-Gyu Park*, "Unique scattering properties of silicon nanowires embedded with porous segments," *ACS Appl. Mater. Interfaces* 11, 21094-21099 (2019).
5. Jungkil Kim, Ha-Reem Kim, Hoo-Cheol Lee, Kyoung-Ho Kim, Min-Soo Hwang, Jung Min Lee, Kwang-Yong Jeong, and Hong-Gyu Park*, "Photon-triggered current generation in chemically-synthesized silicon nanowires," *Nano Letters* 19, 1269-1274 (2019).
6. M. F. Haque, P. Snapp, J. M. Kim, M. C. Wang, H. J. Bae, C. Cho, and S. Nam*, "Strongly Enhanced Electromechanical Coupling in Atomically Thin Transition Metal Dichalcogenides," *Materials Today*, DOI: 10.1016/j.mattod.2020.12.021 (2021).
7. C. Cho, J. Wong, A. Taqieddin, S. Biswas, N. R. Aluru, S. Nam*, and H. A. Atwater, "Highly Strain-Tunable Interlayer Excitons in MoS_2/WSe_2 Heterobilayers," *Nano Letters* 9, 3956 (2021).
8. C. Cho, P. Kang, A. Taqieddin, Y. Jing, K. Yong, J. M. Kim, M. F. Haque, N. R. Aluru, and S. Nam*, "Strain-resilient Electrical Functionality in Thin-film Metal Electrodes using Two-dimensional Interlayers," *Nature Electronics* 4, 126 (2021).
9. C. Choi, J. Leem, M. S. Kim, A. Taqieddin, C. Cho, K. W. Cho, G. J. Lee, H. Seung, H. J. Bae, Y. M. Song, T. Hyeon, N. R. Aluru, S. Nam*, and D.-H. Kim, "Curved Neuromorphic Image Sensor Array using a MoS2-organic Heterostructure Inspired by the Human Visual Recognition System," *Nature Communications* 11, 5934 (2020).
10. P. Snapp, C. Cho, D. Lee, M. F. Haque, S. Nam*, and C. Park, "Tunable Piezoelectricity of Multifunctional Boron Nitride Nanotube/Polydimethylsiloxane Stretchable Composites," *Advanced Materials* 32, 2004607 (2020).
11. Peter Snapp, Jin Myung Kim, Chullhee Cho, Juyoung Leem, Md Farhadul Haque, and SungWoo Nam*, "Interaction of 2D Materials with Liquids: Wettability, Electrochemical Properties, Friction, and Emerging Directions," *NPG Asia Materials* 12, 22 (2020).
12. Keong Yong, Subhadeep De, Ezekiel Y. Hsieh, Juyoung Leem, Narayana R. Aluru, and SungWoo Nam*, "Kirigami-Inspired Strain-Insensitive Sensors based on Atomically-Thin Materials," *Materials Today* 34, 58 (2020).
13. Jin Myung. Kim, Chullhee Cho, Ezekiel Y. Hsieh, and SungWoo Nam*, "Heterogeneous Deformation of Two-dimensional Materials for Emerging Functionalities," *Journal of Materials Research* 35, 1369 (2020).
14. Hyo Chan Lee, Ezekiel Y. Hsieh, Keong Yong, and SungWoo Nam*, "Multiaxially-Stretchable Kirigami-Patterned Mesh Design for Graphene Sensor Devices," *Nano Research* 13, 1406 (2020).
15. Richard Hahnkee Kim, Juyoung Leem, Christopher Muratore, SungWoo Nam, Rahul Rao, Ali Jawaid, Michael Durstock, Michael McConney, Lawrence Drummy, Rachel Rai, Andrey Voevodin, and Nicholas Glavin, "Photonic Crystallization of Two-dimensional MoS2 for Stretchable Photodetectors," *Nanoscale* 11, 13260 (2019). *Selected as the Inside Front Cover.
16. Peter Snapp, Pilgyu Kang, Juyoung Leem, and SungWoo Nam*, "Colloidal Photonic Crystal Strain Sensor Integrated with Deformable Graphene Phototransducer," *Advanced Functional Materials* 33, 1902216 (2019). *Selected as the Frontispiece.
17. Anirudh Krishna, Jin Myung Kim, Juyoung Leem, Michael Cai Wang, SungWoo Nam*, and Jaeho Lee, "Ultraviolet to Mid-Infrared Emissivity Control by Mechanically Reconfigurable Graphene," *Nano Letters* 19, 5086 (2019).
18. Juyoung Leem, Yeagun Lee, Michael Cai Wang, Jin Myung Kim, Jihun Mun, Md Farhadul Haque, SangWoo Kang, and SungWoo Nam*, "Crack-assisted, Localized Deformation of van der Waals Materials for Enhanced Strain Confinement," *2D Materials* 6, 044001 (2019).
19. Sun Sang Kwon, Jonghyun Choi, Mohammad Heiranian, Yerim Kim, Won Jun Chang, Peter Knapp, Michael Cai Wang, Jin Myung Kim, Narayana R. Aluru, Won Il Park, and SungWoo Nam*, "Electrical Double Layer of Supported Atomically-thin Materials," *Nano Letters* 19, 4588 (2019).
20. Pilgyu Kang, Kyoung-Ho Kim, Hong-Gyu Park*, and SungWoo Nam*, "Mechanically Reconfigurable Architectured Graphene for Tunable Plasmonic Resonances," *Light: Science & Applications (Nature)* 7, 17 (2018).

b) papers published in peer-reviewed conference proceedings,
c) papers published in non-peer-reviewed journals and conference proceedings,
d) conference presentations without papers,
e) manuscripts submitted but not yet published, and
f) provide a list any interactions with industry or with Air Force Research Laboratory scientists or significant collaborations that resulted from this work.

- PIs Nam and Park visited AFRL on September 29, 2017 to meet with and explore collaborations with Drs. Ruth Pachter, Shin Mou, Nicholas Glavin and Christopher Tabor.
- PI Nam and Dr. Nicholas Glavin (AFRL)'s collaborative manuscript is published in Nanoscale (R. H. Kim, J. Leem, C. Muratore, S. Nam, R. Rao, A. Jawaid, M. Durstock, M. McConney, L. Drummy, R. Rai, A. Voevodin, and N. Glavin " Photonic Crystallization of Two-dimensional MoS2 for Stretchable Photodetectors," *Nanoscale* 11, 13260 (2019)).
- Dr. Nicholas Glavin and PI Nam are continuing collaborations on sample exchange (Dr. Glavin is providing BN films to PI Nam) and also device measurements.
- Dr. Sarah Holcomb from Dr. Christopher Tabor's team has visited PI Nam's laboratory on December 19-20, 2017 to collaborate on liquid metal contacts to corrugated 2D materials.

Attachments: Publications a), b) and c) listed above if possible.

DD882: As a separate document, please complete and sign the inventions disclosure form.